VLTI/GRAVITY observations and characterization of the brown dwarf companion HD 72946 B

Balmer, W.O.; Pueyo, L.; Stolker, T.; Reggiani, H.; Maire, A.-L.; Lacour, S.; ... ; Young, A.

The Astrophysical Journal, 956:99 (24pp), 2023 October 20 https://doi.org/10.3847/1538-4357/acf761

VLTI/GRAVITY Observations and Characterization of the Brown Dwarf Companion HD 72946 B

William O. Balmer[1,2,32], Laurent Pueyo[2], Tomas Stolker[3], Henrique Reggiani[4,33], A.-L. Maire[5,6], S. Lacour[7,8], P. Mollière[6], M. Nowak[9], D. Sing[1,10], N. Pourré[11], S. Blunt[12], J. J. Wang[13], E. Rickman[14], J. Kammerer[2], Th. Henning[6], K. Ward-Duong[15], R. Abuter[8], A. Amorim[16,17], R. Asensio-Torres[6], M. Benisty[11], J.-P. Berger[11], H. Beust[11], A. Boccaletti[7], A. Bohn[3], M. Bonnefoy[11], H. Bonnet[8], G. Bourdarot[11,18], W. Brandner[6], F. Cantalloube[19], P. Caselli[18], B. Charnay[7], G. Chauvin[11], A. Chavez[13], E. Choquet[19], V. Christiaens[20], Y. Clénet[7], V. Coudé du Foresto[7], A. Cridland[3], R. Dembet[8], J. Dexter[21], A. Drescher[18], G. Duvert[11], A. Eckart[22,23], F. Eisenhauer[18], F. Gao[24], P. Garcia[17,25], R. Garcia Lopez[6,26], E. Gendron[7], R. Genzel[18], S. Gillessen[18], J. H. Girard[2], X. Haubois[27], G. Heißel[7], S. Hinkley[28], S. Hippler[6], M. Horrobin[22], M. Houllé[19], Z. Hubert[11], L. Jocou[11], M. Keppler[6], P. Kervella[7], L. Kreidberg[6], A.-M. Lagrange[7,11], V. Lapeyrère[7], J.-B. Le Bouquin[11], P. Léna[7], D. Lutz[18], J. D. Monnier[29], D. Mouillet[11], E. Nasedkin[6], T. Ott[18], G. P. P. L. Otten[30], C. Paladini[27], T. Paumard[7], K. Perraut[11], G. Perrin[7], O. Pfuhl[8], J. Rameau[11], L. Rodet[31], G. Rousset[7], Z. Rustamkulov[10], J. Shangguan[18], T. Shimizu[18], J. Stadler[18], O. Straub[18], C. Straubmeier[22], E. Sturm[18], L. J. Tacconi[18], E. F. van Dishoeck[3,18], A. Vigan[19], F. Vincent[7], S. D. von Fellenberg[18], F. Widmann[18], E. Wieprecht[18], E. Wiezorrek[18], T. Winterhalder[8], J. Woillez[8], S. Yazici[18], A. Young[18]

The ExoGRAVITY Collaboration

and

The GRAVITY Collaboration

[1] Department of Physics & Astronomy, Johns Hopkins University, 3400 N. Charles St., Baltimore, MD 21218, USA; wbalmer1@jhu.edu
[2] Space Telescope Science Institute, 3700 San Martin Dr., Baltimore, MD 21218, USA
[3] Leiden Observatory, Leiden University, P.O. Box 9513, 2300 RA Leiden, The Netherlands
[4] The Observatories of the Carnegie Institution for Science, 813 Santa Barbara St., Pasadena, CA 91101, USA
[5] STAR Institute/Université de Liège, Belgium
[6] Max Planck Institute for Astronomy, Königstuhl 17, D-69117 Heidelberg, Germany
[7] LESIA, Observatoire de Paris, PSL, CNRS, Sorbonne Université, Université de Paris, 5 place Janssen, F-92195 Meudon, France
[8] European Southern Observatory, Karl-Schwarzschild-Straße 2, D-85748 Garching, Germany
[9] Institute of Astronomy, University of Cambridge, Madingley Rd., Cambridge CB3 0HA, UK
[10] Department of Earth & Planetary Sciences, Johns Hopkins University, Baltimore, MD, USA
[11] Université Grenoble Alpes, CNRS, IPAG, F-38000 Grenoble, France
[12] Department of Astronomy, California Institute of Technology, Pasadena, CA 91125, USA
[13] Center for Interdisciplinary Exploration and Research in Astrophysics (CIERA) and Department of Physics and Astronomy, Northwestern University, Evanston, IL 60208, USA
[14] European Space Agency (ESA), ESA Office, Space Telescope Science Institute, 3700 San Martin Dr., Baltimore, MD 21218, USA
[15] Department of Astronomy, Smith College, Northampton MA 01063, USA
[16] Universidade de Lisboa—Faculdade de Ciências, Campo Grande, 1749-016 Lisboa, Portugal
[17] CENTRA—Centro de Astrofísica e Gravitação, IST, Universidade de Lisboa, 1049-001 Lisboa, Portugal
[18] Max Planck Institute for Extraterrestrial Physics, Giessenbachstraße 1, D-85748 Garching, Germany
[19] Aix-Marseille Université, CNRS, CNES, LAM, Marseille, France
[20] School of Physics and Astronomy, Monash University, Clayton, VIC 3800, Melbourne, Australia
[21] JILA and Department of Astrophysical and Planetary Sciences, University of Colorado, Boulder, CO 80309, USA
[22] 1st Institute of Physics, University of Cologne, Zülpicher Straße 77, D-50937 Cologne, Germany
[23] Max Planck Institute for Radio Astronomy, Auf dem Hügel 69, D-53121 Bonn, Germany
[24] Hamburger Sternwarte, Universität Hamburg, Gojenbergsweg 112, D-21029 Hamburg, Germany
[25] Universidade do Porto, Faculdade de Engenharia, Rua Dr. Roberto Frias, 4200-465 Porto, Portugal
[26] School of Physics, University College Dublin, Belfield, Dublin 4, Ireland
[27] European Southern Observatory, Casilla 19001, Santiago 19, Chile
[28] University of Exeter, Physics Building, Stocker Rd., Exeter EX4 4QL, UK
[29] Astronomy Department, University of Michigan, Ann Arbor, MI 48109, USA
[30] Academia Sinica, Institute of Astronomy and Astrophysics, 11F Astronomy-Mathematics Bldg., NTU/AS Campus, No. 1, Sec. 4, Roosevelt Rd., Taipei 10617, Taiwan
[31] Center for Astrophysics and Planetary Science, Department of Astronomy, Cornell University, Ithaca, NY 14853, USA
Received 2023 June 15; revised 2023 August 25; accepted 2023 September 5; published 2023 October 12

[32] Johns Hopkins University George Owen Fellow.
[33] Carnegie Fellow.

Abstract

Tension remains between the observed and modeled properties of substellar objects, but objects in binary orbits, with known dynamical masses, can provide a way forward. HD 72946 B is a recently imaged brown dwarf companion to a nearby, solar-type star. We achieve $\sim$100 μas relative astrometry of HD 72946 B in the K band using VLTI/GRAVITY, unprecedented for a benchmark brown dwarf. We fit an ensemble of measurements of the orbit using `orbitize!` and derive a strong dynamical mass constraint $M_B = 69.5 \pm 0.5\ M_{\rm Jup}$ assuming a strong prior on the host star mass $M_A = 0.97 \pm 0.01\ M_\odot$ from an updated stellar analysis. We fit the spectrum of the companion to a grid of self-consistent `BT-Settl-CIFIST` model atmospheres, and perform atmospheric retrievals using `petitRADTRANS`. A dynamical mass prior only marginally influences the sampled distribution of effective temperature, but has a large influence on the surface gravity and radius, as expected. The dynamical mass alone does not strongly influence retrieved pressure–temperature or cloud parameters within our current retrieval setup. Independently of the cloud prescription and prior assumptions, we find agreement within $\pm 2\sigma$ between the C/O of the host (0.52 ± 0.05) and brown dwarf (0.43–0.63), as expected from a molecular cloud collapse formation scenario, but our retrieved metallicities are implausibly high (0.6–0.8) in light of the excellent agreement of the data with the solar-abundance model grid. Future work on our retrieval framework will seek to resolve this tension. Additional study of low surface gravity objects is necessary to assess the influence of a dynamical mass prior on atmospheric analysis.

Unified Astronomy Thesaurus concepts: Brown dwarfs (185); L dwarfs (894); Interferometry (808); Long baseline interferometry (932); Optical interferometry (1168); Orbit determination (1175); Exoplanet atmospheres (487); Stellar atmospheres (1584)

1. Introduction

Brown dwarfs (BDs) are substellar objects unable to fuse hydrogen ($M \lesssim 75$–$80\ M_{\rm Jup}$; Saumon & Marley 2008; Baraffe et al. 2015; Dupuy & Liu 2017; Fernandes et al. 2019). Due to their insufficient mass, their cores do not reach the temperatures required for nuclear fusion to balance radiative losses, and they become supported by electron degeneracy pressure (Chabrier & Baraffe 2000). BDs burn away deuterium (and lithium, for $M \gtrsim 65\ M_{\rm Jup}$; Dupuy & Liu 2017; Zhang et al. 2019), soon exhausting this relatively scarce fuel, and cool "inexorably like dying embers plucked from a fire" (Burrows et al. 2001). The known population of BDs are rich in spectral diversity (Cushing et al. 2005) because their lack of nuclear heating leads to low effective temperature atmospheres with dense, overlapping molecular opacities that evolve over time as the BD continues to cool. This complexity necessitates precise luminosity, age, and mass measurements in order to properly test models of BD evolution and composition. This is much easier said than done.

Theories of star formation suggest that a significant number of higher-mass BDs form via molecular cloud collapse during the process of star formation, either alone, in binary pairs, or near stellar-mass hosts, but undergo subsequent ejection (e.g., Padoan 2004; Bate 2009; Umbreit et al. 2005). It is still vigorously debated whether or not (or, more realistically, what proportion of) low-mass BDs arise from the fragmentation of the circumstellar disk around more massive stars (Boss 1997; Stamatellos et al. 2007; Stamatellos & Whitworth 2009; Kratter et al. 2010; Li et al. 2016; Squicciarini et al. 2022), and in what ways these processes are related to planet formation. Around main-sequence FGK stars, a "brown dwarf desert" exists (Grether & Lineweaver 2006), where few BD companions can be found at solar system scale separations (Ma & Ge 2014). New work appears to reveal similar trends, scaled up or down in mass, around earlier-type stars (Duchêne et al. 2023) and late-type (even substellar) objects (Fontanive et al. 2018). This makes known companions of this nature, inhabitants of the desert, interesting in the broader context of BD studies.

Moreover, the similarity (in physics, chemistry, and composition) between BDs and giant planets has motivated the careful study of these objects, particularly of their atmospheres, as more readily accessible laboratories for studying the physics of giant planets. Giant planets span the L–T–Y spectral sequence of BDs, and in many ways our current modeling of directly detected super-Jovian exoplanet atmospheres depends on models and observations of BDs (Bowler 2016). Many evolutionary and spectral models exist (e.g., Burrows et al. 1997; Allard et al. 2003; Saumon & Marley 2008; Allard et al. 2013; Baraffe et al. 2015; Phillips et al. 2020), but the degeneracy between BD age and mass (as younger, less massive BDs can appear as hot and luminous as older, more massive BDs) has complicated the process of testing these models, as masses cannot be independently determined for isolated field BDs.

BDs in binary orbits around main-sequence stars are important to study for two key reasons. First, because a combination of radial velocities (RVs) and astrometry (relative and/or absolute) can yield their dynamical mass (e.g., Dupuy & Liu 2017; Brandt et al. 2019, 2021; Fontanive et al. 2019; Rickman et al. 2020, 2022; Bonavita et al. 2022; Franson et al. 2022, 2023; Li et al. 2023), a model-independent mass determination can be derived from orbital motion. Second, because we expect binaries that form via molecular cloud collapse to exhibit similar chemical compositions, and because BD interiors are fully convective (Chabrier & Baraffe 2000), we can test our ability to retrieve atmospheric abundances for substellar companions on these objects of approximately known composition (that is, provided disequilibrium effects in the atmosphere do not impede our ability to infer the composition, as the composition throughout the BD interior is not distinct from the composition of the atmosphere). This is not the case, for example, for planets formed via core accretion, where a rocky core might enrich the atmosphere with metals (e.g., Thorngren & Fortney 2019). For these "benchmark" companions to stars, we can measure the abundances of the host and compare them to the abundances derived for the more opaque (physically and theoretically) atmosphere of the substellar object. Many spectral modeling frameworks are

benchmarked against one another, but not against these benchmark BDs, whose dynamical mass is known after measuring their motion in a binary orbit, and whose composition is assumed to be approximately stellar. There is an emerging body of work, which this paper contributes to, that attempts to detect benchmark candidates, measure their dynamical masses, observe their atmospheres, apply existing evolutionary models to the benchmarks to check for consistency, and finally test the vast array of atmospheric model codes against objects of known mass (Line et al. 2015; Peretti et al. 2019; Wang et al. 2022; Xuan et al. 2022).

1.1. A Sequence of Ls: Difficulty in Modeling Clouds?

The observed population of directly imaged young giant planets follow the L-type sequence of spectral types (Bowler 2016; see their Figure 7), and so the study of L-type BDs well motivates those seeking to understand the atmospheres of directly imaged giant planets. This sequence is distinguished by the presence of carbon monoxide (CO)-dominated atmospheres, whose near-infrared (NIR) colors redden as they become fainter. The challenge of accurately modeling atmospheres in the L-type regime is the apparent presence of condensate clouds. The influence of these clouds was first observed in the NIR color–magnitude relation for BDs, as later-type L dwarfs become increasingly red before the L–T transition, where condensate clouds no longer dominate NIR colors for field BDs (e.g., Knapp et al. 2004; Dupuy & Liu 2012). Additionally, the presence of these clouds can be inferred directly, by measuring the absorption due to cloud grains in the mid-infrared (MIR) (e.g., Suárez & Metchev 2022, 2023), or indirectly, via the impact of cloud opacity on the shape of the spectral slope of shorter wavelengths, or via variability studies that indicate the rotation of patchy clouds in and out of view (e.g., Vos et al. 2022).

The carbon-to-oxygen ratio (C/O) of an object is theorized to encode information about the formation location or history of giant exoplanets, assuming the form, composition, and evolution of the circumstellar disk (Öberg et al. 2011). As demonstrated in, e.g., Mollière et al. (2022) the actual practice of linking C/O to the formation history of a given planet is challenging because these planet formation model assumptions can strongly influence the interpretation of a given measured C/O. For young, massive directly imaged planets inhabiting the L dwarf sequence, even obtaining accurate measurements of this quantity is confounded by the presence of clouds. Indeed, in conducting an analysis of two late-T dwarf companions (whose atmospheres may be less strongly affected by the same kinds of clouds than those of L dwarfs), Line et al. (2015) found good agreement between the retrieved abundances of BDs and their hosts. This has been more difficult to reproduce for L dwarfs.

Burningham et al. (2017) analyzed the L4 spectral template 2MASS J05002100+0330501, and the L4 dwarf 2MASSW J2224438-015852, both field objects. They identified major disagreement between their CO abundance and the solar abundance, and they noted that future work focusing on benchmark L dwarfs may be necessary to rigorously test their ability to retrieve gas abundances. Interestingly, Peretti et al. (2019) found similar disagreement when studying the SPHERE *YJH* spectrum and *K*-band photometry of the benchmark L9 BD HD 4747 B. They derived a dynamical mass of 65.3 ± 4.4 $M_{\rm Jup}$ from RV measurement and direct imaging, and used retrieval analysis to identify C and O abundances that are discrepant with their measured abundances for the host star HD 4747 A. They noted, however, that spectroscopic measurements of the object in the *K* band, at the 2.29 μm CO absorption band, are needed to truly constrain these abundances.

Gonzales et al. (2020) conducted a retrieval analysis of the L7+T7 binary SDSS J1416+1348AB, where they recovered an equivalent C/O between the binary pair. Wang et al. (2022) analyzed a high spectral resolution observation of the benchmark L-type BD HR 7672 B, a close-in companion to the solar-type star HR 7672 A, with the Keck Planet Imager and Characterizer (KPIC). They found elemental abundances consistent with the primary star using an extension of the `petitRADTRANS` code (see our description in Section 5.2 for references). Xuan et al. (2022), also using KPIC in conjunction with `petitRADTRANS`, found C and O abundances derived for HD 4747 B in exceptional agreement, and a C/O only discrepant at the 2σ level with its host star. They cited the uncertainty in stellar abundances (due to non-LTE effects) or the sequestration of O in cloud condensates makes up the difference.

1.2. HD 72946: A High-contrast L5 Benchmark

HD 72946 A is a bright, nearby star ($G = 7.02$ mag, $d = 25.87 \pm 0.08$ pc; Gaia Collaboration et al. 2021). It is comoving with the spectroscopic binary HD 72945 AB, at a separation of $\sim 10''$ (Gaia Collaboration et al. 2021). From high-resolution optical spectroscopy, Bouchy et al. (2016) measured a $T_{\rm eff} = 5686 \pm 40$ K, $\log g = 4.50 \pm 0.06$ dex, and $[{\rm Fe/H}] = 0.11 \pm 0.03$ dex stellar atmosphere. Various studies corroborate a supersolar metallicity (e.g., Luck & Heiter 2006; Casagrande et al. 2011; Aguilera-Gómez et al. 2018). Luck (2017) found a stellar C/O ~ 0.5. Maire et al. (2020) conducted an analysis of available data in order to determine the age of the system, and found a range of 0.8–3 Gyr, with a most probable value of 1–2 Gyr from a combination of lithium data, stellar kinematics, isochronal analysis, and a rough gyrochronological estimate. Brandt et al. (2021) conducted a similar age analysis, using a "Bayesian activity age method," from which they derived a posterior distribution of $1.9^{+0.6}_{-0.5}$ Gyr, in agreement with Maire et al. (2020).

In 2016, Bouchy et al. reported an RV signal, measured using the ELODIE and SOPHIE instruments, that was best fit by a low-mass companion with minimum mass $M \sin(i) = 60.4 \pm 2.2$ $M_{\rm Jup}$ and a ~ 16 yr period. The RV data covered the full phase of the companion's orbit. Subsequently, the companion was directly imaged using the VLT/SPHERE instrument (Maire et al. 2020). Maire et al. jointly fit the RV measurements with both their SPHERE relative astrometry and absolute astrometry from the Hipparcos–Gaia Catalog of Accelerations (HGCA; Brandt 2018), assuming a stellar mass prior of 0.986 ± 0.027 $M_\odot$ based on their isochronal analysis. They derived a dynamical mass of 72.4 ± 1.6 $M_{\rm Jup}$ for the companion, confirming its substellar nature. They computed $\log L_{\rm bol}/L_\odot = -4.11 \pm 0.10$ dex by converting their SPHERE/IFS *J*-band magnitude into a J_s magnitude and applying the empirical relation in Filippazzo et al. (2015).

With updated absolute astrometry from Gaia eDR3 (Gaia Collaboration et al. 2021), adopting the same stellar mass prior as Maire et al. (2020), Brandt et al. (2021) computed an orbital

Table 1
Observing Log

Date	UT		NEXP/NDIT/DIT (s)		Airmass	τ_0 (ms)	Seeing (arcsec)	Fiber Pointing ΔR.A., ΔDecl.	γ
	Start	End	HD 72946 B	HD 72946 A					
2020-02-09	05:11:28	05:36:55	2/8/60	3/64/1	1.22–1.28	5.2–6.0	0.68–0.95	151.9, 153.4	0.968
2021-01-05	05:37:04	06:12:42	2/8/100	3/64/1	1.17–1.19	2.5–4.2	0.96–1.36	157.0, 101.0	0.999
2021-01-30	06:09:31	07:03:12	3/8/100	4/64/1	1.27–1.46	2.1–2.9	1.09–1.45	155.6, 100.3	0.991
2022-01-25	05:01:25	05:26:05	2/16/30	3/64/1	1.17–1.18	6.2–8.1	0.57–0.74	156.5, 38.0	0.994

Notes. NEXP, NDIT, and DIT denote the number of exposures, the number of detector integrations per exposure, and the detector integration time, respectively, and τ_0 denotes the atmospheric coherence time. The fiber pointing is the placement of the science fiber relative to the fringe tracking fiber (which is placed on the central star), and γ is the coupling efficiency at the position of the companion (see Table 2).

solution that gives $M_B = 72.5 \pm 1.3\ M_{\rm Jup}$. They used the computed dynamical mass to benchmark three evolutionary models: Burrows97 (Burrows et al. 1997), SM08-hybrid (Saumon & Marley 2008), and ATMO2020 (Phillips et al. 2020). They computed $\log L_{\rm bol}/L_\odot = -4.133 \pm 0.023$ dex by computing the Maunakea Observatories and Two Micron All Sky Survey (2MASS) photometry of the best-fit template found in Maire et al. (2020) and using the relation in Dupuy & Liu (2017). They used the measured age and bolometric luminosity to derive a model mass, and the measured mass and bolometric luminosity to derive model ages. They found the age for HD 72946 B to be consistent with predictions from SM08-hybrid and ATMO2020, but discrepant by 1.4σ with the Burrows et al. (1997) models. This discrepancy is expected, as those models are cloud-free. They interpreted their results as evidence that HD 72946 B's substellar cooling age is in agreement with its host's age.

Despite its relatively recent discovery and close separation, HD 72946 B is becoming an important benchmark for BDs near the hydrogen-burning limit. This work presents new observations of HD 72946 B in the *K* band using the Very Large Telescope Interferometer (VLTI)/GRAVITY instrument, and seeks to demonstrate GRAVITY's exceptional ability to improve studies of benchmark objects. We then seek to prove HD 72946 B's utility as a spectral benchmark by interrogating the atmospheric retrieval codes employed in the study of L-type exoplanets by the ExoGRAVITY Large Program (Lacour et al. 2019).

2. Observations and Data Reduction

2.1. VLTI/GRAVITY

We observed HD 72946 B on 2020 February 9, on 2021 January 1 and 30, and on 2022 January 25 (UTC) using the European Southern Observatory (ESO) VLTI's four 8.2 m unit telescopes and the GRAVITY instrument (Gravity Collaboration et al. 2017) in fringe tracking mode (Lacour et al. 2019). The observations were carried out as target visibility and bad weather backups to the ExoGRAVITY Large Program (ESO program ID 1104.C-0651; Lacour et al. 2020). The observing log, presented in Table 1, records the length of the observations and the number of files. The atmospheric conditions were rather good during most of the observations. The placement of the science fiber was based on preliminary orbit fits to the available relative astrometry and RVs of the system (Maire et al. 2020) and is reported in Table 1, along with the analytical coupling efficiency at the location of the companion (a function of the distance between the companion location and the fiber pointing; see Appendix A in Wang et al. 2021). The coupling efficiency was >95% for all observations, so we did not correct for its effect on the observed spectra.

We extracted the complex visibilities on the host and the companion, which were phase-referenced with the metrology system, for each observation using Public Release 1.5.0 (2021 July 1[34]) of the ESO GRAVITY pipeline (Lapeyrere et al. 2014). We then decontaminated flux on the companion due to the host using a custom Python pipeline developed by our team. This pipeline is described in detail in Appendix A of Gravity Collaboration et al. (2020).

We obtained astrometry for each epoch by analyzing the phase of the ratio of the coherent fluxes. Briefly, our pipeline generated a χ^2 periodogram power map over the fiber's field of view (FOV) (Figure 1). The astrometry was taken to be the minimum of the χ^2 map. We estimated the uncertainty on each astrometric point from the rms of the astrometric values fit to each individual exposure.[35] Then, the pipeline extracted the ratio of coherent fluxes between the two sources, i.e., the "contrast spectrum" of the companion, which is robust to variations in atmospheric quality and instrument stability (Nowak et al. 2020), at the location of the companion.

The relative astrometry is listed in Table 2. For GRAVITY observations, we give the R.A. and decl. positions and their uncertainties as measured, in addition to the correlation coefficient that describes the elliptical confidence interval (CI). The extracted spectrum, the contrast spectrum multiplied by a synthetic host spectrum (see Section 3), is shown in Figure 2.

2.2. Previous Observations of HD 72946

We obtained the optical stellar spectrum used in Section 3 and the RVs of HD 72946 A published in Bouchy et al. (2016) through the ELODIE and SOPHIE archives[36] (Moultaka et al. 2004). The spectrum used to determine HD 72946 A's stellar parameters was observed on 2008 March 12, and has a signal-to-noise ratio ≈150 at 5000 Å.

We obtained the HGCA eDR3 edition (Brandt 2021) within orbitize! (Blunt et al. 2020) on a branch of the orbitize! GitHub that automates retrieval of the HGCA.[37]

[34] https://www.eso.org/sci/software/pipelines/gravity/

[35] The typical precision is on the order of ∼100 μas ≫ 16.5 μas (the theoretical limit of VLTI/GRAVITY), due to high- and low-frequency phase errors induced by instrumental systematics.

[36] atlas.obs-hp.fr/sophie/

[37] Our orbit fit including the proper-motion anomaly used a development version of orbitize! recorded in commit 5ffc5c0 (http://github.com/sblunt/orbitize/commit/5ffc5c01cd5318bce2b17392bec12578f8f5dcb4) from 2022 May.

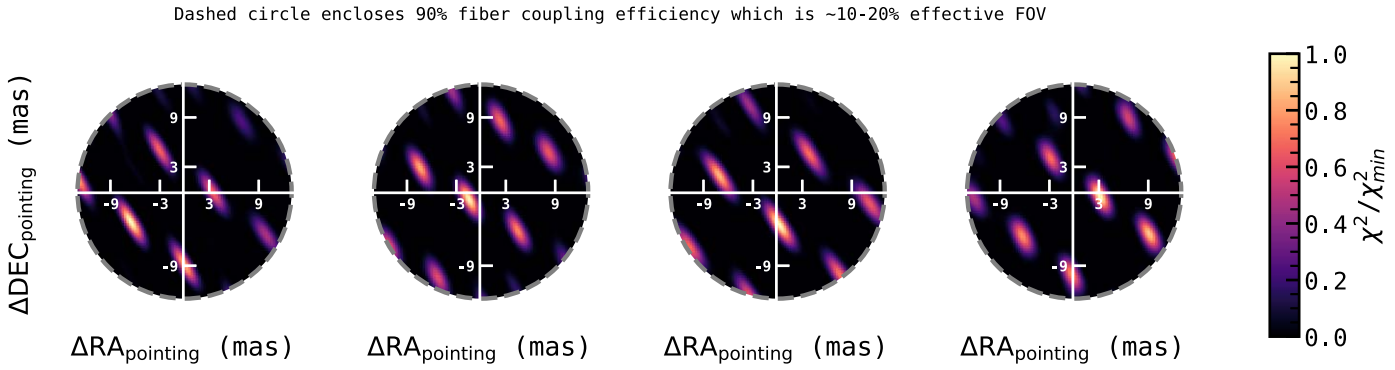

Figure 1. Detections of HD 72946 B with VLTI/GRAVITY. Each panel visualizes the periodogram χ^2 map calculated after subtracting the stellar residuals. Each epoch in Table 1 is presented chronologically, left to right. The dashed gray circle indicates the radius beyond which the coupling efficiency into the instrument fiber is <90% (this is much smaller than the complete fiber FOV, which is ∼60 mas). The origin is the placement of the science fiber on-sky for a given observation, a prediction based on the previous available orbit fit. The strongest peak in the χ^2 map indicates the position of the companion, with characteristic interferometric side lobes whose shape and distribution depend on the *u*–*v* plane coverage.

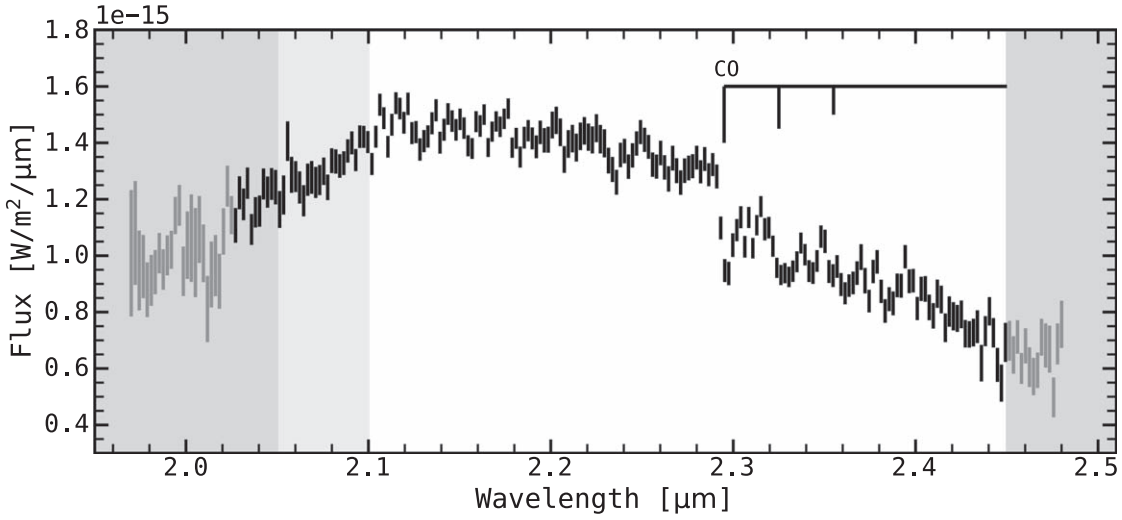

Figure 2. The *K*-band spectrum of HD 72946 B. The flux-calibrated companion spectrum is a weighted combination of the four observed contrast spectra, multiplied by the flux-calibrated host spectrum (Figure 13). The error bars represent the diagonal of the full covariance matrix. The 2.29 μm carbon monoxide bandhead is indicated, and regions of poor atmospheric transmission are shaded gray (Vacca et al. 2003). The gray data points are excluded from our atmospheric model fits.

Table 2
New Relative Astrometry of HD 72946 B around HD 72946 A

GRAVITY					
Epoch (MJD)	ΔR.A. (mas)	$\sigma_{\Delta R.A.}$ (mas)	ΔDecl. (mas)	$\sigma_{\Delta Decl.}$ (mas)	ρ
58,888.22	145.54	0.08	149.92	0.12	−0.8165
59,219.24	155.64	0.02	100.24	0.04	0.0253
59,244.27	155.95	0.06	96.41	0.06	−0.500
59,604.22	159.67	0.04	37.78	0.0	−0.8825

Note. The covariance matrix can be reconstructed using $\sigma^2_{\Delta R.A.}$ and $\sigma^2_{\Delta Decl.}$ on the diagonal, and using $\rho \times \sigma_{\Delta R.A.} \times \sigma_{\Delta Decl.}$ on the off-diagonal.

We also made use of previous direct detections of the companion with the SPHERE instrument in the *Y*, *J*, and *H* bands (Maire et al. 2020). We included their epoch of relative astrometry in our orbital analysis and the spectrophotometry in our spectral analysis. We did not re-reduce the data, and adopted the values recorded in Maire et al. (2020), except that we used their spectrophotometric contrast measurements (as opposed to their absolute flux measurements) and transformed them into absolute flux measurements using a synthetic host spectrum based on our analysis in Section 3, in order to be consistent with the absolute flux we determined for the VLTI/GRAVITY spectrum. We propagated uncertainties in quadrature, and decided to inflate the uncertainty estimates of the *H*-band photometry, and the last seven blue spectral channels in the *Y*–*J* spectrophotometry. We justify this on the basis that the blue channels in the SPHERE data suffer from significantly decreased throughput as compared to the red channels, and that the *H*-band photometry likely includes correlated noise that, unlike the spectroscopic data sets, we could not account for via a correlation matrix. For the last seven blue spectral channels in the *Y*–*J* spectrophotometry, we added the median uncertainty in quadrature with the median uncertainty estimate from the remaining channels. We similarly inflated the uncertainty on the H1 and H2 photometry by a factor of 3.5 (from $\pm 1.36 \cdot 10^{-17}\,\mathrm{W\,m^{-2}\,\mu m^{-1}}$ to $\pm 4.88 \cdot 10^{-17}\,\mathrm{W\,m^{-2}\,\mu m^{-1}}$), adding the median uncertainty from reliable *Y*–*J* channels in quadrature to the median *H*-band photometric uncertainties.

3. Host Analysis

In order to properly assess the properties of HD 72946 B, we conducted an up-to-date analysis of the host star. We sought to determine the most precise mass possible for the host. While our orbit fits that include the proper-motion anomaly will technically weigh the host as well as the companion, our knowledge of the host's properties from isochronal and spectroscopic modeling can place a much stronger constraint on the host mass (and therefore aid in a more precise mass determination for the companion). Since we are also interested in the abundances of the BD, we sought to measure the abundances of the host, primarily the stellar C/O. Although HD 72946 A is a solar-neighborhood, solar-type star, assuming solar abundances without verification can lead to wrong conclusions (see, e.g., Reggiani et al. 2022 for details on one such cautionary tale).

3.1. Stellar Parameters

Using the algorithm outlined in Reggiani et al. (2022) we obtained the host star's fundamental and photospheric parameters. Our analysis makes use of both the classical spectroscopy-only approach[38] and isochrones to infer accurate, precise, and self-consistent photospheric and fundamental stellar parameters. The method improves the composition determination by leveraging the isochrones to help determine the effective temperature and surface gravity using archival photometry and Gaia parallax, while the spectrum determines the abundances and microturbulence parameters.

The inputs to our photospheric and fundamental stellar parameter inference include the EWs of the Fe I and Fe II atomic absorption lines. The absorption line data are from Yana Galarza et al. (2019) for the lines from Meléndez et al. (2014) are found to be insensitive to stellar activity. We measured the EWs by fitting Gaussian profiles with the `splot` task in `IRAF` (Tody 1986, 1993) to our continuum-normalized spectrum. Whenever necessary, we used the `deblend` task to disentangle absorption lines from adjacent spectral features. We included multiwavelength photometry (Gaia Data Release 3 (DR3) G; 2MASS J, H, and K_s; and Tycho B and V) and Gaia DR3 parallax (Høg et al. 2000; Skrutskie et al. 2006; Gaia Collaboration et al. 2016, 2018; Fouesneau et al. 2023). We assumed Asplund et al. (2021) solar abundances and followed the steps described in Reggiani et al. (2022) to obtain the fundamental and photospheric stellar parameters of the host star from a combination of spectral information and a fit to MESA Isochrones and Stellar Tracks (MIST; Paxton et al. 2011, 2013, 2015, 2018, 2019; Choi et al. 2016; Dotter 2016). We performed the fitting through the `isochrones` package[39] (Morton 2015), which uses `MultiNest`[40] (Feroz & Hobson 2008; Feroz et al. 2009, 2019) via `PyMultiNest` (Buchner et al. 2014). In particular, the parameters were computed via efficient interpolations across the MIST grid space and precomputed synthetic photometry for each isochrone was compared to the observed photometry of the star. The updated Gaia parallax provides a well-constrained surface gravity, and the broad-wavelength photometric coverage constrains the effective temperature. These lead to a precise mass estimate. As a consistency check we also employed the *colte*[41] code (Casagrande et al. 2021) to estimate the stellar effective temperature via the infrared flux method (IRFM). The IRFM effective temperature is $T_{\rm eff} = 5592 \pm 71$ K, fully consistent with our adopted effective temperature. Our adopted fundamental and photospheric parameters are displayed in Table 3.

Table 3
Adopted Stellar Parameters

Property	Value	Unit
Gaia DR3 G	7.024 ± 0.002	Vega mag
2MASS J	5.882 ± 0.024	Vega mag
2MASS H	5.609 ± 0.027	Vega mag
2MASS K_s	5.497 ± 0.021	Vega mag
Tycho B	7.933 ± 0.02	Vega mag
Tycho V	7.159 ± 0.02	Vega mag
Gaia DR3 parallax	9.459 ± 0.056	mas
Isochrone-inferred parameters		
Effective temperature $T_{\rm eff}$	5638 ± 14	K
Surface gravity $\log g$	4.51 ± 0.01	cm s^{-2}
Stellar mass M_*	0.97 ± 0.01	$M_\odot$
Stellar radius R_*	0.91 ± 0.01	$R_\odot$
Luminosity L_*	0.77 ± 0.01	$L_\odot$
Spectroscopically inferred parameters		
$[{\rm Fe/H}]_{\rm 1D\ LTE}$	0.036 ± 0.023	⋯
$[{\rm Fe/H}]_{\rm 1D\ non\text{-}LTE}$	0.069 ± 0.080	⋯
$({\rm C/O})_{\rm 1D\ LTE}$	$0.512^{+0.047}_{-0.043}$	⋯
$({\rm Mg/Si})_{\rm 1D\ LTE}$	1.047 ± 0.124	⋯
ξ	0.98 ± 0.09	km s^{-1}
Age estimates		
Isochrone-based age $\tau_{\rm iso}$	$2.67^{+0.25}_{-0.49}$	Gyr
[Y/Mg]-based age	1.9 ± 1.5	Gyr
[Y/Al]-based age	$0.5^{+1.5}_{-0.5}$	Gyr

3.2. Chemical Composition of HD 72946 A

We inferred the elemental abundances of C I, Na I, Mg I, Al I, Si I, Ca I, Sc I, Sc II, Ti I, Ti II, V I, Cr I, Cr II, Fe I, Fe II, Ni I, Cu I, Zn I, Sr I, Sr II, Y II, Zr II, Ba II, Ce II, and Dy II from the EWs of the absorption lines. The EWs were measured from our continuum-normalized spectrum by fitting Gaussian profiles with the `splot` task in `IRAF`. We used the `deblend` task to disentangle absorption lines from adjacent spectral features whenever necessary. We assumed Asplund et al. (2021) solar abundances and LTE and used the 1D plane-parallel solar-composition ATLAS9 model atmospheres and the 2019 version of `MOOG` (Sneden 1973; Sneden et al. 2012) to infer elemental abundances based on each EW measurement.

SOPHIE spectra have a wavelength range of 3900–6940 Å, which does not include the oxygen triplet at 7771–7775 Å. Therefore, our oxygen abundance comes from the forbidden oxygen transition at 6300.3 Å. This transition is blended with a nickel line, and to obtain the abundance one must synthesize the spectral region (e.g., Teske et al. 2014). We used the *linemake*[42] code (Sneden et al. 2009, 2016; Placco et al. 2021) to create a linelist for our analysis, and we updated the atomic

[38] The classical spectroscopy-only approach to photospheric stellar parameter estimation involves simultaneously minimizing individual line-based iron abundances and inferring the difference between Fe I and Fe II–based abundances as well as their dependencies on the transition excitation potential and measured reduced equivalent width (EW).
[39] github.com/timothydmorton/isochrones
[40] ccpforge.cse.rl.ac.uk/gf/project/multinest/
[41] github.com/casaluca/colte
[42] github.com/vmplacco/linemake

data of the oxygen and nickel transitions according to Johansson et al. (2003) and Magg et al. (2022). As these transitions are not strong transitions, and due to the spectral quality at the region, our quoted oxygen abundance should be viewed as a lower limit. The optical spectrum of HD 72946 A covering the oxygen triplet region would allow us to determine a definitive oxygen abundance.

Whenever possible we also applied line-by-line abundance corrections for non-LTE effects and 3D effects. We applied 1D non-LTE corrections for aluminum (Amarsi et al. 2020), calcium (Amarsi et al. 2020), and iron (Amarsi et al. 2016). We also made use of 3D non-LTE corrections for carbon (Amarsi et al. 2019). We present our full set of chemical abundances, including the non-LTE corrected abundances, in Table 7.

3.3. Stellar Age

The isochrone-based age of the host star is $\tau = 2.67^{+0.25}_{-0.49}$ Gyr. As HD 72946 A is part of the thin disk, it also follows the same chemistry–age relations, determined via different chemical clocks, that were derived using large samples of solar twins in the solar neighborhood. We applied the chemical clocks from Spina et al. (2016) and found $\tau_{[Y/Mg]} = 1.9 \pm 1.5$ Gyr and $\tau_{[Y/Al]} = 0.5^{+1.5}_{-0.5}$ Gyr.

We note the agreement between this age and the 0.8–3 Gyr estimate made by Maire et al. (2020). Our [Y/Mg] age agrees well with the $1.9^{+0.6}_{-0.5}$ Gyr estimate from Brandt et al. (2021), but our isochrone-based age is slightly older. For this work we adopt the isochrone-based age of $\tau = 2.67^{+0.25}_{-0.49}$ Gyr, because it is consistent with the other fundamental stellar parameters determined here.

3.4. Synthetic Stellar Spectrum

In order to transform the contrast spectra measured for HD 72946 B with GRAVITY and SPHERE, we used `species` (Stolker et al. 2020) to scale a `BT-NextGen` (Allard et al. 2012) synthetic stellar spectrum with the inferred parameters we derived above to the archival photometry (see Table 3). In order to scale the spectrum, we let the radius float while fixing all other parameters to their inferred values, except for the parallax—we placed a Gaussian prior around the Gaia parallax. The resulting radius is consistent with our inferred radius to within 1σ uncertainties, and the residuals to the fit are within 2.5σ for each photometric measurement (see Appendix B, Figure 13), which we take as validation that the BT-NextGen model is an appropriate synthetic spectrum to use in order to generate our absolute flux calibrated companion spectra. We sampled the spectrum at the resolution of the GRAVITY and SPHERE spectra using `spectres` (Carnall 2017), and over the bandpass of the SPHERE H-band photometry using `synphot` (STScI Development Team 2018). We found that at the resolution of the $R = 500$ GRAVITY data, reasonable changes in the stellar properties produce no noticeable change in the absolute-fluxed spectrum of the companion, and any line depth variations due to the (nonsolar) abundances of the host are negligible at this resolution. To test the impact systematic errors in our assumed stellar properties would have on our flux-calibrated spectrum of HD 72946 B, we tested the difference using a synthetic stellar spectrum with $T_{\rm eff}$ set to the IRFM effective temperature derived in Section 3.1; we found that the two spectra based on independently derived $T_{\rm eff}$ produced a negligible difference compared to the uncertainties on the contrast spectrum itself.

4. Orbit Analysis

We now have four new astrometric observations of HD 72946 B at a precision unprecedented for a "benchmark" BD (Table 2). This exquisite precision ($\sim$30$\times$ more precise than previous imaging) allows us to determine the orbital parameters for the object very finely. In both analyses we conducted, we included the SPHERE and GRAVITY relative astrometry, as well as the SOPHIE and ELODIE RVs. In one analysis, we excluded the proper-motion anomaly and parallax data, fitting for only RVs and relative astrometry. In another analysis, we included the proper-motion anomaly measurements from the HGCA and the parallax from Gaia in the fit.

We used the parallel-tempered (Vousden et al. 2016) affine-invariant (Foreman-Mackey et al. 2013) Markov Chain Monte Carlo (MCMC) algorithm packaged within `orbitize!`[43] that fits for the six-parameter visual orbit (Green 1985); the system parallax, offset, and jitter terms for each RV instrument; and the masses of the star and companion. We placed a physically motivated normally distributed prior $\mathcal{N}(0.97\ M_{\odot}, 0.03\ M_{\odot})$ on the mass of the primary based on the isochronal analysis conducted in Section 3, and otherwise implemented default priors on all orbital elements as described in Blunt et al. (2020). In the analysis excluding the proper-motion anomaly, we set a uniform prior ($\pm$1 mas) around the system parallax and allowed the MCMC to converge on the parallax naturally. In the analysis including the proper-motion anomaly, we set a tight prior on the Gaia eDR3 parallax recorded for the system $\mathcal{N}(38.981$ mas, 0.041 mas) following Brandt et al. (2021) to facilitate comparison with their work.

We initialized `orbitize!` with 50 walkers and 20 temperatures, and ran 200,000 steps that were discarded as "burn-in" before 20,000 were accepted to estimate the posterior distribution, for a total of 11,000,000 orbits fit. We visually inspected the chains to check for convergence. Figure 3 visualizes the marginalized posterior distributions of the masses of the host and companion for both cases. The full posterior distribution of orbital elements for both cases is visualized in Appendix A, Figure 10. The median and 1σ uncertainty on the orbital parameters derived from the posterior distribution of fits are reported in Appendix A, Table 5, for the fit without the proper-motion anomaly and in Table 6 for the fit with the proper-motion anomaly.

Figure 4 plots the relative astrometry in Table 2 with 50 randomly drawn orbits from the posterior distribution of orbital fits, illustrating the refined orbit achieved by combining a full phase of RV measurements and incredibly precise on-sky astrometry.

The orbital period of the system ($\sim$16 yr) is short enough that there is significant nonlinear motion of the primary and secondary components over the Gaia observing baseline. There may be errors in the parallax/proper-motion fit for eDR3 for a host star like HD 72946 A because of this orbital motion. This can be solved with the addition of the per-scan epoch astrometry, or with a parallax fit assuming a binary solution (as was done for the system in DR3). For this reason, because we conducted the analysis using the eDR3 data, we fit two cases of orbits, one with and one without the proper-motion

[43] orbitize.readthedocs.io

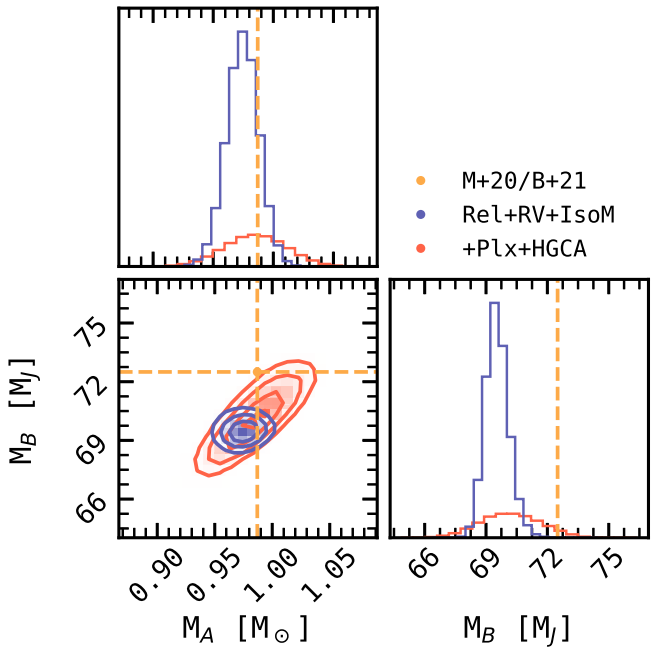

Figure 3. The posterior distribution of the masses of HD 72946 A and B from the orbit fits conducted in this work, compared to literature values. The fits excluding the proper-motion anomaly and parallax (red) and including the proper-motion anomaly (blue) are plotted against the median values reported in Maire et al. and Brandt et al. (the single orange line, as the central values in both are effectively equivalent). We find a best-fit mass $M_B = 69.5^{+0.5}_{-0.5}\,M_{\rm Jup}$, still consistent with previous results within 1σ–2σ, but $\sim$2 $M_{\rm Jup}$ lower. In all works, M_A is effectively fixed by a strong prior based on an isochronal analysis of the primary star. Notably, our revised primary mass is slightly lower than that used in previous works, which explains the subsequent offset in secondary mass.

anomaly. When fitting including the proper-motion anomaly, we used measurements of the proper-motion anomaly from the eDR3 HGCA, which strategically inflates the Gaia errors to avoid biasing the orbit fit. This appears to work well, leading to an increased precision on our mass that still agrees with our fit that excludes absolute astrometry, but we present the fit without absolute astrometry for completeness.

We find primary and secondary masses slightly lower than those in Brandt et al. (2021), but still in agreement at 2σ. This is attributable to our revised host analysis, which slightly lowered the primary star mass estimate. Our semimajor axis and eccentricity also largely agree with their values. The precise GRAVITY astrometry effectively fixes the semimajor axis in our fits, and the RVs provide a significant period constraint, leading to a refinement in the remaining free parameter in Kepler's equation, the mass, as well as in the on-sky orientation of the ellipse.

Excluding absolute astrometry we find a secondary mass error of 3.134%, while including it we find a secondary mass error of 1.129%. In either case, this strong dynamical mass constraint makes HD 72946 B a standout benchmark candidate for the L5 class and for high-mass BDs in general. Fitting with epoch astrometry (to be released in Gaia DR4) could work to push the uncertainty on the secondary mass below 1% for this object.

Using the isochronal age from Section 3 and our updated dynamical mass, we compared the age and mass of HD 72946 B to two evolutionary models (one cloudless, one cloudy), primarily to determine the expected radius for the BD. Our updated dynamical mass and isochronal age are not entirely inconsistent with previous findings (Maire et al. 2020; Brandt et al. 2021), and so we do not repeat their benchmarking analysis (for instance, comparing marginalized combinations of the bolometric luminosity, age, and dynamical mass samples to a variety of evolutionary models to check for consistency) in this paper. Based on our dynamical mass and age estimates we computed the effective temperature, surface gravity, radius, and bolometric luminosity of HD 72946 B using the cloudless Sonora Bobcat model (Marley et al. 2021) and the cloudy ($f_{\rm sed} = 2$) SM08 model (Saumon & Marley 2008). Both models assume solar metallicity. We drew 10,000 random samples from the posterior distributions on the dynamical mass and the isochronal age, and computed the corresponding parameters from each evolutionary model grid by interpolating linearly between grid points using the `species` package (Stolker et al. 2020).

We find an estimate of the radius of HD 72946 B of $0.89 \pm 0.01\,R_{\rm J}$ for the cloudy SM08 model and of $0.84 \pm 0.02\,R_{\rm J}$ for the cloudless Sonora Bobcat model. The estimated effective temperatures are 1567 ± 70 K and 1470 ± 52 K, respectively.

5. Spectral Analysis

Having nearly doubled the wavelength coverage for HD 72946 B with the addition of our GRAVITY observations, we conducted an initial atmospheric analysis using both a self-consistent grid of model atmospheres and an atmospheric inversion (a "retrieval") of a model atmosphere. Throughout, we were predominately interested in leveraging the dynamical mass to more accurately fit for atmospheric parameters. We generally avoided constructing models that would require intensive computational resources (e.g., free temperature or pressure node profiles), which we postpone to future work. Here, we present a qualitative exploration of the new data and an overview of the atmospheric properties we computed for HD 72946 B.

5.1. Self-consistent `BT-Settl` Model Grid

In order to investigate the atmosphere of HD 72946 B we began by comparing the observed spectrum to a self-consistently produced grid of model atmospheres. The `BT-Settl-CIFIST` grid was chosen because of its microphysical cloud treatment for L-type BDs (Allard et al. 2003, 2011, 2013; Baraffe et al. 2015). We expected the model grid to provide good results for an old, high surface gravity BD based on the excellent match the model has demonstrated to the observed moderate ($R = 3000$) spectra of the L5.5 field BD 2MASS 1507-16 (see Figure 1 of Allard 2014). The model performs admirably for young, low surface gravity BDs but like other models, it struggles to reproduce the H-band slope and J-band flux of L dwarfs (Bonnefoy et al. 2010; Patience et al. 2012; Manjavacas et al. 2014), and overpredicts the effective temperature and underpredicts the radius as compared to evolutionary models.

We used the `species` package to fit the `BT-Settl-CIFIST` grid, linearly interpolating spectra between grid points. We initialized UltraNest[44] (Buchner 2019, 2021) via `species` to sample the interpolated grid with 500 live points.

[44] johannesbuchner.github.io/UltraNest/

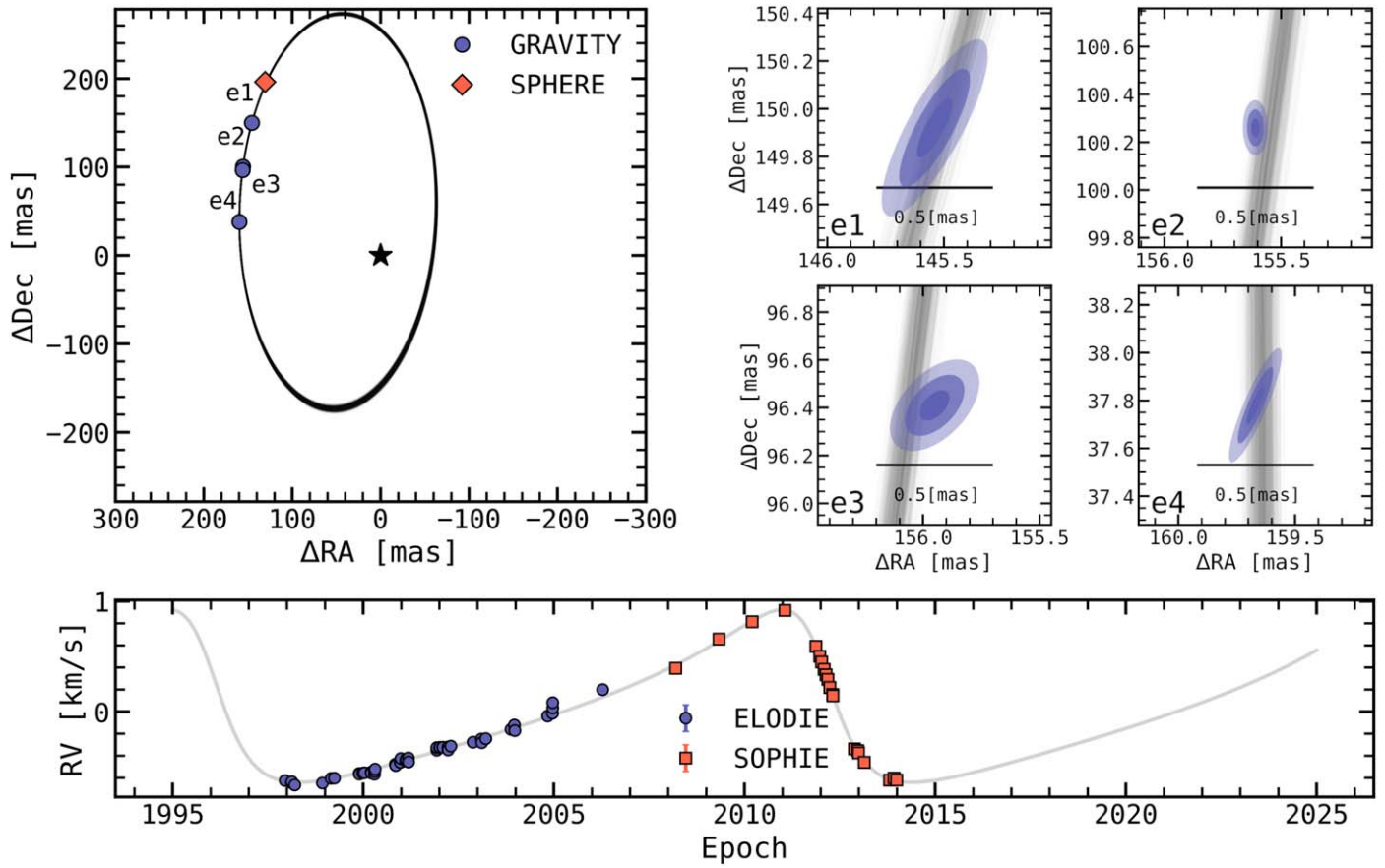

Figure 4. The orbit of HD 72946 B. Top left: One hundred randomly drawn orbits from the posterior of orbital fits made using `orbitize!` are plotted in R.A. and decl. relative to HD 72946 A (black star); overplotted are the direct detections of HD 72946 B from VLT/SPHERE and VLTI/GRAVITY, whose error bars are too small to visualize at this scale. Each GRAVITY detection is labeled e1–e4 in chronological order. Top right: GRAVITY astrometry on HD 72946 B is overplotted against the 100 randomly drawn orbits. The semitransparent lines represent the 1σ errors on the astrometry in R.A./decl. reported in Table 2, while the solid ellipses represent the 1σ, 2σ, and 3σ confidence determined by the correlation coefficient (also in Table 2), which fully describes the confidence on the astrometry. Lower panel: RVs of HD 72946 A from ELODIE and SOPHIE (Bouchy et al. 2016), overplotted against 50 of the randomly drawn orbits in the above panels.

We measured the posterior distribution on the grid parameters, namely the effective temperature ($T_{\rm eff}$), log(g), radius, and parallax, and included a Gaussian process parameterized by a squared-exponential kernel to account for correlated noise between wavelength channels in the SPHERE data (see Section 4.1 in Wang et al. 2020). When fitting the GRAVITY data, `species` accounts for the correlation matrix of the spectrum in the fit.

To investigate its discerning power, we fit the `BT-Settl-CIFIST` grid to the data twice, first without a prior on the mass of the object, and then assuming a Gaussian prior on the mass equivalent to the dynamical mass we derived in Section 4. Effectively, this experiment let the sampler determine the log (g) and radius based only on the spectral measurements, and then constrained the log(g) and radius based on the dynamical mass. Figure 5 plots the best-fit `BT-Settl-CIFIST` model.

Even using UltraNest, which implements a "safer" uncertainty estimation than other nested sampling packages (Nelson et al. 2020), the uncertainties on the physical parameters derived here are likely underestimated due to systematic errors between the various grids of self-consistent models and unaccounted-for sources of error in the spectra (for instance, uncorrected higher-order telluric or instrumental effects). That being said, the experiment yielded two distinct solutions for the atmospheric parameters: the constrained mass favored a slightly cooler, higher surface gravity solution, while the free mass estimated a slightly hotter, lower surface gravity solution. The free mass maximum a posteriori spectrum yielded a higher-log evidence, with a $\Delta \ln Z = 50 \pm 0.5$ as compared to the mass prior fit. The difference between the two cases appears small, especially considering the inability of the implemented sampling methods to estimate systematic errors. Nevertheless, the difference in log(g) is significant when given the statistical uncertainties ($\Delta\log(g) = 0.22$, $\delta \log(g) \simeq 0.02$), and results in a mass discrepant from our dynamical mass by 32 $M_{\rm Jup}$. The posterior distribution of effective temperatures is discrepant with those derived from both a cloudless and a cloudy evolutionary model (see Table 4). Interestingly, with the inclusion of the dynamical mass prior, the spectroscopically inferred radius is shifted toward agreement with the evolutionary models.

The posteriors for both fits (Figure 11 in Appendix A) are well behaved and effectively Gaussian. We report the median and 1σ CI on each parameter in Table 4 for both fits. The best-fit parameters from the dynamical mass constrained fit give a total luminosity of $\log L/L_{\odot} = -4.15$.

The `BT-Settl` self-consistent models provide an excellent fit to the data. While the model appears to be a marginally poor fit to the 0.95–1.05 μm slope of the SPHERE data, it captures the SPHERE and especially the GRAVITY spectrum remarkably well, and with solar abundances. Small deviations could be due to data deficiencies (residual telluric contamination or

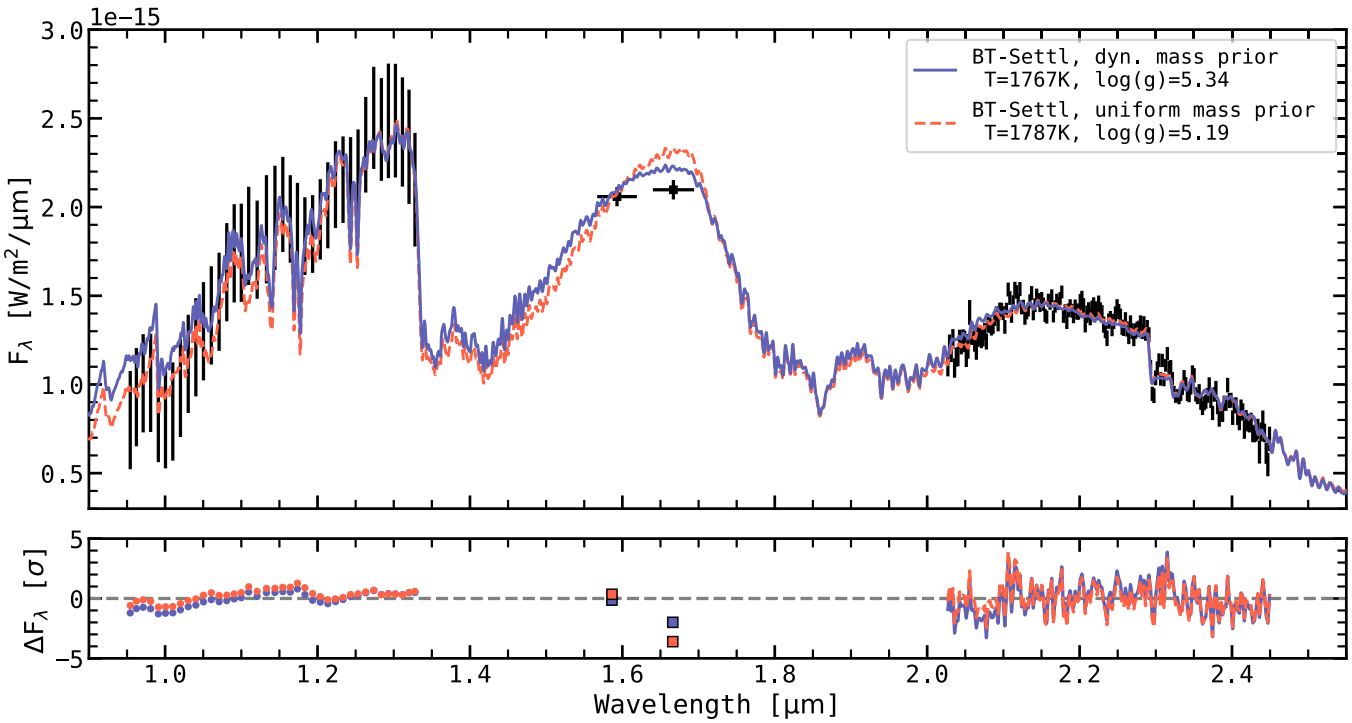

Figure 5. The observed spectrum of HD 72946 B fit to the `BT-Settl` grid. The best-fit model spectrum assuming the dynamical mass is plotted as a solid blue curve, while the fit with mass as a free parameter is plotted as a dashed red curve; both models have been smoothed to $R = 500$. The SPHERE/IFU spectrum, SPHERE/IRDIS photometry, and GRAVITY spectrum are plotted in black, from left to right. The residuals to each fit are plotted below, and show some non-Gaussian structure. In particular, the SPHERE *Y*–*J* spectral slope appears to be in tension with the model. Aside from a noticeable underluminosity near 2.05 μm, the residuals to the GRAVITY spectrum are relatively normally distributed.

poorly corrected instrumental throughput) or model deficiencies. Notably, there is systematic uncertainty involved when linearly interpolating spectra between widely spaced grid points, because line or molecular feature depths do not vary linearly with temperature or surface gravity (Czekala et al. 2015). Our experiment proves the usefulness of the dynamical mass as an independent physical prior, as it helped the sampler avoid overfitting less reliable regions of the observation (or model), and constrained the $\log(g)$ in the absence of a strong spectral constraint on the *H*-band slope, which is sensitive to variations in surface gravity.

5.2. `petitRADTRANS` Retrievals

While precomputed grids of model atmospheres can treat the interrelation between the pressure–temperature (P-T) structure of the atmosphere, particle clouds, and the chemistry self-consistently from first principles, in order to determine the precise atmospheric abundances of the atmosphere it is necessary to make a number of assumptions and conduct an atmospheric inversion, or "retrieval," where rapidly computed model atmospheres based on simplifying assumptions are sampled from a posterior space and compared to the data.

We selected the open-source `petitRADTRANS` (Mollière et al. 2019) radiative transfer code to perform our atmospheric retrievals. The code has been used to conduct retrievals of young, low surface gravity objects (e.g., HR 8799 e, β Pic b; Mollière et al. 2020; Nowak et al. 2020) successfully, capturing the slopes and absorption features of spectra well, as well as retrieving reasonable cloud properties, with the usual caveats concerning effective temperatures and radii, which are incongruous compared to expectations from evolutionary models. Despite its success with directly imaged planets, and despite having been benchmarked against self-consistent models, the code remains relatively untested for older, higher surface gravity objects in the literature. We used `species` as a wrapper for `petitRADTRANS`, and the scripts used to generate the retrievals presented herein are available upon request.[45] The `species` retrieval implementation used `pyMultiNest` (Feroz et al. 2009; Buchner et al. 2014) to sample model parameters before passing these parameters to `petitRADTRANS` to generate a model spectrum by solving the radiative transfer equation, and then compared the model spectrum to the data.

To limit computational expense, in this initial retrieval reconnaissance we ran `petitRADTRANS` in constant sampling efficiency mode. Unfortunately, this choice limited our ability to intercompare the likelihood and posterior probability of each retrieval. We intended instead to qualitatively explore a handful of questions informed by the retrievals.

We refer the reader to Mollière et al. (2020) for more details, but attempt to describe the most essential elements of the retrieval here. In general, our `petitRADTRANS` retrievals assumed abundances are in chemical equilibrium. We included CO, H_2O, CH_4, NH_3, CO_2, Na, K, TiO, VO, FeH, and H_2S line species and collision-induced absorption (CIA) of H_2 and He. The line opacities were taken from the ExoMolOP database (Chubb et al. 2021), in the "petitRADTRANS" format,[46] while the CIA opacities were from Borysow et al. (1988, 1989, 2001) and Richard et al. (2012). The abundances were parameterized

[45] A generalized retrieval example can be found online at species.readthedocs.io.
[46] www.exomol.com

Table 4
Subset of Parameters for HD 72946 B Derived from Evolutionary and Atmospheric Analysis

Model	Notable Parameters								$\chi^2_{\rm red}$/d.o.f.
	Mass ($M_{\rm Jup}$)	$T_{\rm eff}$ (K)	log(g)	Radius ($R_{\rm J}$)	(Fe/H)	C/O	Cloud Parameters		log($L/L_\odot$)	
Evolutionary										
Sonora Bobcat	69.5 ± 0.5	1567 ± 70	5.38 ± 0.02	0.84 ± 0.02	solar	solar	cloudless		-4.39 ± 0.09	⋯
SM08 (cloudy)	69.5 ± 0.5	1470 ± 52	5.33 ± 0.01	0.89 ± 0.01	solar	solar	$f_{\rm sed} = 2$		-4.45 ± 0.07	⋯
Self-consistent (forward model)										
`BT-Settl-CIFIST`, $\mathcal{U}(M_B)$	37.52 ± 2.52	1790 ± 5	5.17 ± 0.02	0.79 ± 0.01	solar	solar	microphysical		-4.15 ± 0.01	1.36/228
`BT-Settl-CIFIST`, $\mathcal{N}(M_B)$	69.5 ± 0.5	1770 ± 4	5.39 ± 0.01	0.84 ± 0.01	solar	solar	microphysical		-4.140 ± 0.005	1.58/228
Atmospheric inversion (retrieval)										
`petitRADTRANS` cloudless										
$\mathcal{N}(M_B)$	69.5 ± 0.5	1656 ± 18	5.29 ± 0.02	0.94 ± 0.02	0.86 ± 0.05	0.63 ± 0.01	...	...	-4.20 ± 0.01	1.51/221
`petitRADTRANS` gray cloud							log($\kappa_{\rm gray}$)	log($P_{\rm top}$)		
$\mathcal{N}(M_B)$	69.5 ± 0.5	1720 ± 20	5.39 ± 0.02	0.86 ± 0.01	0.69 ± 0.05	0.58 ± 0.01	2.20 ± 1.60	0.52 ± 0.03	-4.21 ± 0.01	1.50/219
`petitRADTRANS` EddySed							$f_{\rm sed}$	log(K_{zz})		
$\mathcal{U}(M_B)$	119^{+50}_{-40}	1868 ± 21	$5.70^{+0.17}_{-0.20}$	0.77 ± 0.02	0.79 ± 0.14	0.58 ± 0.02	14.2 ± 3.4	$3.2^{+0.61}_{-0.55}$	-4.17 ± 0.01	1.42/214
$\mathcal{N}(M_B)$	69.5 ± 0.5	1846 ± 23	5.45 ± 0.02	0.78 ± 0.02	0.72 ± 0.14	0.59 ± 0.02	$15.5^{+2.6}_{-2.9}$	$3.07^{+0.77}_{-0.62}$	-4.16 ± 0.01	1.45/214
$\mathcal{U}(M_B)$, $\mathcal{N}([{\rm Fe/H}]_A,\ {\rm C/O}_A)$	$38.0^{+13.0}_{-8.1}$	1765 ± 16	5.12 ± 0.13	0.85 ± 0.02	0.03 ± 0.01	$0.48^{+0.02}_{-0.03}$	$15.8^{+2.8}_{-3.57}$	$2.63^{+0.43}_{-0.38}$	-4.17 ± 0.01	1.97/214
$\mathcal{N}(M_B)$, $\mathcal{N}([{\rm Fe/H}]_A,\ {\rm C/O}_A)$	69.5 ± 0.5	1785 ± 24	5.39 ± 0.02	0.83 ± 0.02	0.03 ± 0.01	0.43 ± 0.01	$14.0^{+3.4}_{-3.6}$	$2.58^{+0.40}_{-0.36}$	-4.17 ± 0.01	1.58/214

Notes. For each type of model considered (evolutionary, self-consistent atmospheric, or atmospheric inversion) we record the mean and 1σ standard deviation for the parameters of interest. $\mathcal{U}(\mathcal{P})$ or $\mathcal{N}(\mathcal{P})$ denotes a uniformly or normally distributed prior on the parameter P. There are $39 + 193 + 2 - \Sigma P_i = 234 - \Sigma P_i$ degrees of freedom for each spectral fit.

as functions of the C/O and metallicity [Fe/H], as well as of the P-T structures discussed below. As in Section 5.1, we fit for the correlated noise in the SPHERE spectrum, and the GRAVITY spectrum correlation matrix was accounted for in the fit.

5.2.1. P-T Structure

We implemented the "three-part" or Mollière P-T parameterization that is described in Section 2.2 of Mollière et al. (2020). This P-T profile is motivated by the desire to strike a balance between a purely parametric and a purely free P-T structure. This three-part P-T profile splits the pressure space into three regions: at high temperatures there are free pressure nodes, in the photospheric region (between $\tau = 0.1$ and the radiative–convective boundary) we apply the Eddington approximation, and below the radiative–convective boundary (high pressures), we apply a moist adiabat. The moist adiabatic gradient is found by interpolating in the P-T–[Fe/H]–C/O space of the chemistry table, and the atmosphere is forced onto the moist adiabat once it becomes Schwarzschild-unstable. This P-T profile avoids enforcing the isothermal upper atmosphere required by the Eddington approximation, while enjoying the benefits of the approximation, namely the physical motivation, speed of analytic computation, and a reduced number of free parameters. We did not test fully flexible retrievals using free pressure or free temperature nodes (e.g., Wang et al. 2022), even though it has been suggested that rigid analytical retrievals could bias retrieved abundances. We decided not to test fully flexible P-T profile retrievals largely because of their computational intensity. Future work could indeed investigate this assumption using existing data or data of higher spectral resolution, which would prevent overfitting.

5.2.2. Cloud Parameterization

We also investigated the effect of clouds and cloud parameterization on our retrievals. Suárez & Metchev (2022) found that the MIR Spitzer spectra of mid-L-type field BDs have the strongest absorption signatures due to silicate grains at 8–11 μm. These silicates are thought to nucleate clouds, whose opacity dominates the NIR spectra of substellar objects (e.g., Cushing et al. 2006). As HD 72646 B is an L5-type, it is squarely within the peak of the silicate cloud sequence (Suárez & Metchev 2022; see their Figure 6) and thus could reasonably be expected to host silicate clouds. Alternatively, Tremblin et al. (2015, 2016) noted that the NIR spectra of substellar objects can be explained by a reduced temperature gradient generated by diabatic convection driven by thermal and compositional gradients in the atmosphere (Tremblin et al. 2019).

The first and more simplistic cloud model treats the cloud deck as a gray—meaning wavelength-independent—non-scattering absorber, parameterized by the opacity of the cloud, $\log \kappa_{\rm gray}$, and the pressure of the cloud top, $P_{\rm top}$. The physical implications of such a simple cloud model might be overstated, and a more honest interpretation of this simplistic cloud model is that, marginalized over both parameters, it acts to damp the spectrum uniformly across wavelengths.

The second cloud model follows the Ackerman & Marley (2001) parameterization (see Section 2.4 in Mollière et al. 2020 for the implementation of this cloud model in `petitRADTRANS`), which we dub the EddySed model. We included the opacities from Henning & Stognienko (1996) (Fe) and Scott & Duley (1996) and Jaeger et al. (1998) ($MgSiO_3$). This physically motivated model implements absorption and scattering of $MgSiO_3$ and Fe clouds, expected for a BD of these temperatures. We effectively varied the sedimentation efficiency, the vertical mixing of cloud particles, and the particle size distribution by freely sampling the parameters $f_{\rm sed}$, K_{zz}, and σ_g, respectively. In order to enforce a cloudy atmosphere, we used a parameter $\log \tau_{\rm cloud}$ to scale the cloud opacity at the photosphere (where $\tau = 1$). When this parameter was used, instead of retrieving the logarithmic abundance of enstatite ($\log \widetilde{X}_{\rm MgSiO_3}$) and iron ($\log \widetilde{X}_{\rm Fe}$) separately, we retrieved $\log \tau_{\rm cloud}$ and the logarithmic ratio of abundances ($\log \widetilde{X}_{\rm Fe}/\widetilde{X}_{\rm MgSiO_3}$). An example and further discussion of the implementation of this $\log \tau_{\rm cloud}$ parameter can be found in Brown-Sevilla et al. (2023). When running retrievals with clouds, we implemented adaptive mesh refinement, increasing the vertical resolution of the atmosphere about the cloud base in order to resolve the abrupt onset of the cloud deck (Mollière et al. 2020).

5.3. Retrieval Experiments

We sought to test the influence a prior on the dynamical mass of the object has on an atmospheric free retrieval. In principle, a dynamical mass prior indirectly constrains the surface gravity and radius of the atmosphere, but we wanted to test whether this would lead to more accurately retrieved abundances (e.g., abundances similar to the host star's) and whether a dynamical mass prior might help constrain cloud properties. We investigated the role of clouds in the atmosphere, leveraging our dynamical mass prior. Our first retrieval is cloudless, and relies on our flexible P-T profile to reproduce qualitatively the reduced temperature gradient to fit the data. The second implements the "grey""gray" cloud model, and the third the EddySed model. We also sought to test whether placing priors from the stellar abundances ([Fe/H] and C/O) might inform our retrieval of the BD properties. Table 4 records the median and 1σ CI of a subset of the parameters of interest, derived from the retrievals fit to the observed spectrum of HD 72946 B.

Figure 6 shows the 1D marginalized posterior for notable retrieval parameters in our dynamical mass and abundance experiment, while Appendix A, Figure 12, plots the full comparative posterior distributions. Model spectra from our cloud experiment are shown in Figure 7. Model spectra from our dynamical mass and abundance experiment four are shown in Figure 8, illustrating the influence different prior assumptions have on the resulting spectrum. Figure 9 plots the P-T profile for the cloud experiment retrievals.

6. Discussion

Our atmospheric analysis is summarized in Table 4. In general, we expected to be able to construct some model atmosphere that can fit the data arbitrarily well given enough independent free parameters, with or without clouds (see, for instance, the results of Lueber et al. 2022). Instead of comparing the Bayesian evidences for our retrievals (which, in order to do properly, would require running the retrievals with a nonconstant sampling efficiency, which would dramatically increase the computation time required), we sought to

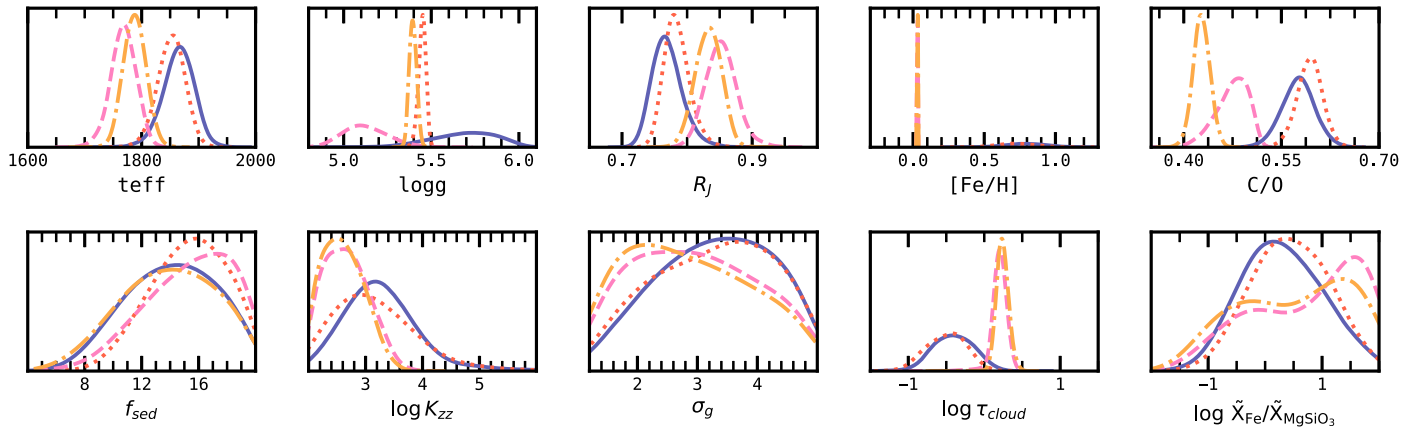

Figure 6. Comparing the 1D marginalized posterior distributions of notable retrieval parameters, for retrievals recorded in Table 4 and illustrated in Figure 8. The uniform mass and abundance prior retrieval is shown as a dotted red curve; the dynamical mass, uniform abundance prior retrieval is shown as a solid blue curve; the uniform mass, stellar abundance prior retrieval is shown as a pink dashed curve; and the dynamical mass and stellar abundance prior retrieval is shown as a dashed–dotted yellow curve. Assuming a dynamical mass does not appear to affect the outcome of the retrieval as dramatically as setting a prior on the abundances. Without an abundance prior, the retrieval estimates C/O that are slightly higher, but still consistent with stellar values, but [Fe/H] that are much higher than stellar (0.8 compared to 0.03). A stellar abundance prior strongly shapes the location of the cloud (log τ_{cloud} is more sharply peaked, and the ratio of cloud particles is shifted toward the prior bounds), whereas for a uniform abundance prior, cloud parameters are more widely distributed.

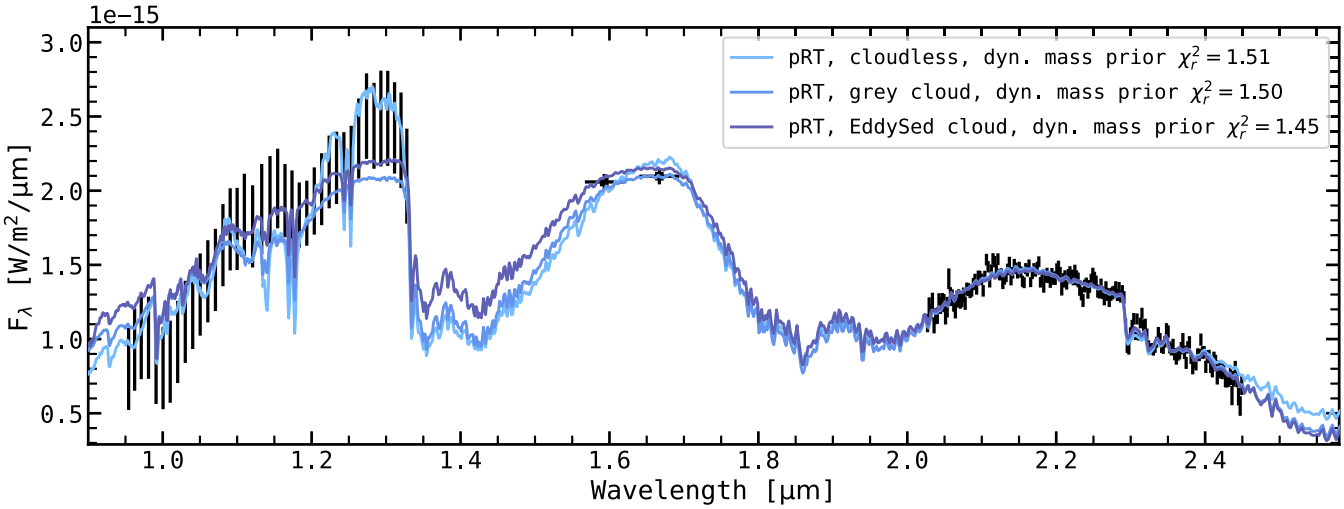

Figure 7. The maximum a posteriori spectra for three retrievals that varied the cloud model, but applied a dynamical mass prior. Observations of HD 72946 B are plotted as in Figure 5. The best-fit retrievals fit the GRAVITY data well in each case, but the choice of cloud model appears to strongly influence the goodness of fit to the SPHERE *Y*–*J* spectrophotometry.

conduct a preliminary qualitative assessment of the BD atmosphere.

We compared our dynamical mass and age estimates to two example evolutionary models, the cloudy SM08 (Saumon & Marley 2008) and the cloudless Sonora Bobcat (Marley et al. 2021), deriving effective temperatures, surface gravities, radii, and luminosities predicted by the dynamical mass (as opposed to inferring a mass via a luminosity and age estimate as is common for non-benchmark objects). We found that in general the effective temperatures from the evolutionary models disagree by about 200–300 K with the effective temperatures from our spectroscopic modeling.

Our observations of HD 72946 B proved an excellent match to a solar-composition, cloudy `BT-Settl-CIFIST` model atmosphere (Section 5.1) with $T_{\rm eff} \sim 1780$ K, but the derived surface gravity and radius were dependent on our inclusion of our dynamical mass as a prior in our fit. Without the dynamical mass, the fit to the model grid derived a lower surface gravity and smaller radius (5.2 and 0.79 R_J, respectively) than the fit with the dynamical mass (5.4 and 0.84 R_J), which led to a wildly incorrect mass determination (37.5 $M_{\rm Jup}$ compared to the 69.5 $M_{\rm Jup}$ dynamical mass). Interestingly, while neither spectroscopic effective temperature agrees with the results from the evolutionary models we explored, our dynamical mass prior run sampled surface gravities consistent with those derived from the cloudy SM08 evolutionary models. This indicates the importance of a dynamical mass prior in assessing model deficiencies for evolutionary and self-consistent atmospheric models.

6.1. Presence of Clouds

We verified the claim made by Tremblin et al. (2015) that the shape of the spectrum can be reproduced with either a cloud opacity or a reduced temperature gradient, by constructing a cloudless, simple-cloud, and EddySed-cloud retrieval

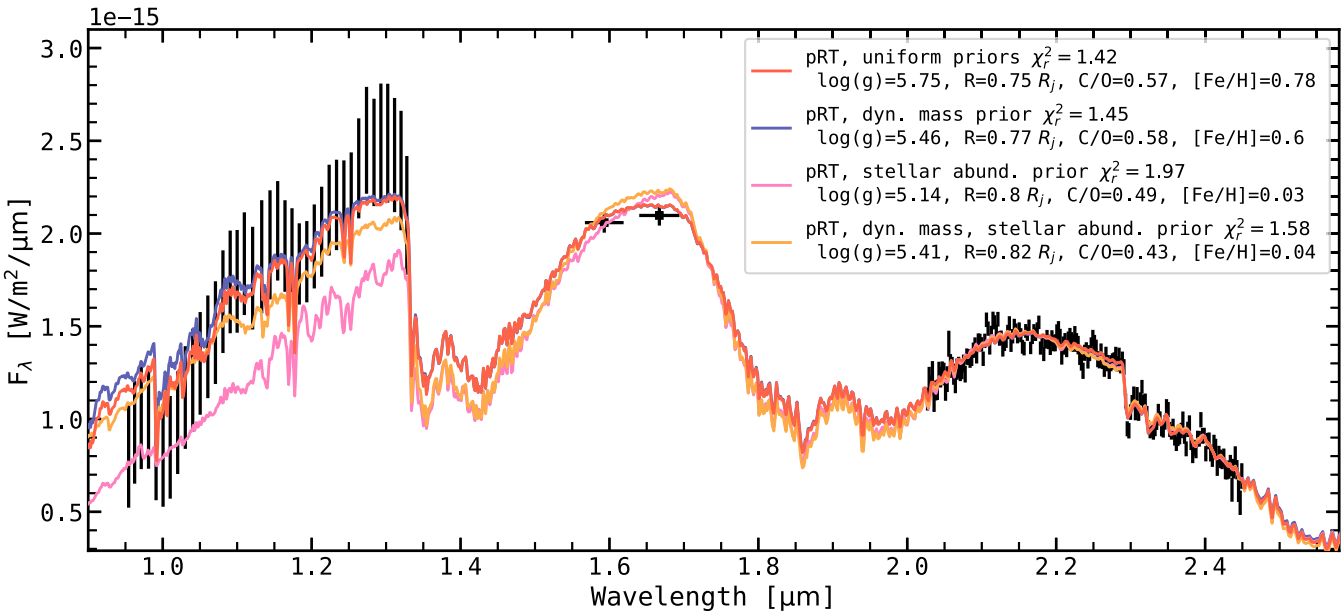

Figure 8. The maximum a posteriori spectra for the four EddySed retrievals, with varying prior assumptions of the mass and abundances of the atmosphere. Observations of HD 72946 B are plotted as in Figure 5. The best-fit retrievals fit the GRAVITY data well in each case, but struggle to capture the slope of the SPHERE *Y*–*J* spectrophotometry.

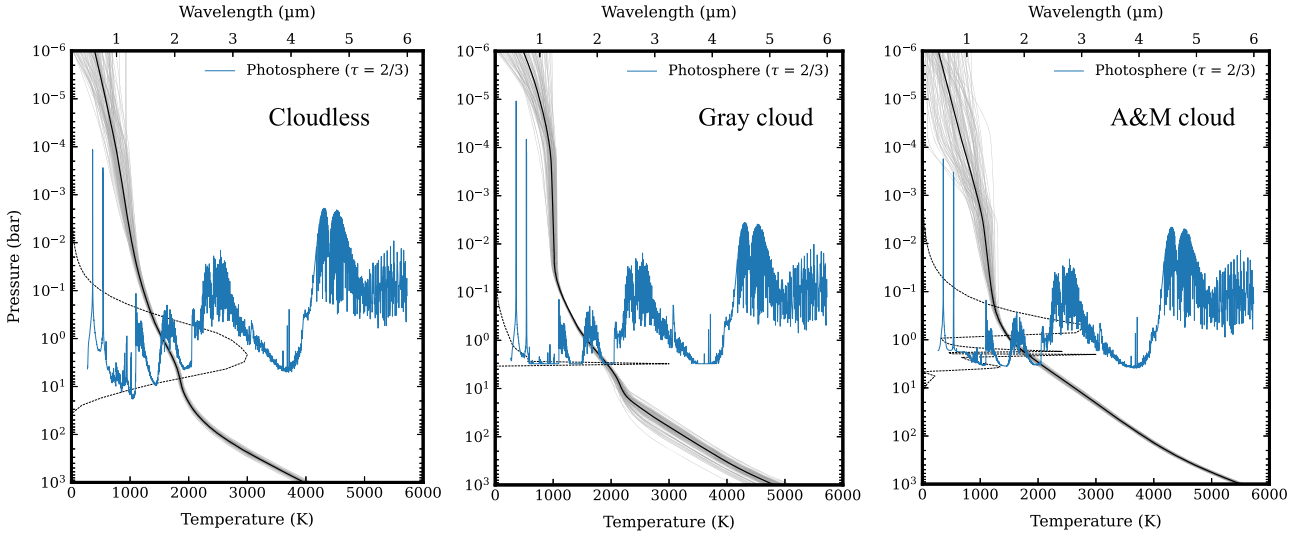

Figure 9. A comparison between the retrieved P-T structure of HD 72946 B using three-part P-T parameterization, fixing the mass to the dynamical mass, but varying the cloud prescription between cloudless conditions (left), a gray slab cloud (middle), and a scattering cloud of iron and enstatite grains parameterized by sedimentation efficiency (right). The ordinate plots the pressure in units of bars. The temperature is shown along the bottom abscissa and corresponds to the black and gray solid curves, while the wavelength is shown along the top abscissa and corresponds to the blue solid curve, which shows the pressure at which the optical depth is 2/3 (e.g., the location in altitude of the photosphere). A 1D histogram of the contribution function is plotted along the left axis as a dotted curve, showing the contribution of a given pressure to the opacity of the atmosphere averaged over all computed wavelengths. Notably, the P-T profile for each retrieval deviates below the photosphere: an iron condensate cloud appears in the EddySed retrieval, the P-T grows more isothermal in the gray cloud retrieval, and the isothermal region becomes larger in the cloudless retrieval.

comparison (see Figure 7). As seen in Figure 9, the simple one-layer cloud model still relies on the flexibility of the P-T profile to reproduce the data with an "isothermal knee," whereas the EddySed model with Fe and $MgSiO_3$ cloud decks shows an approximately Eddington profile even below the photosphere. Each retrieval within this cloud experiment provided an acceptable fit to the data, with $\chi^2_{\rm red} < 2$ and 220–230 degrees of freedom, but because the posteriors were sampled with a constant efficiency, and have differing numbers of free parameters, a rigorous Bayesian intercomparison is not possible.

In general, the cloud parameters converge on similar results, producing a compact cloud layer between 10 and 1 bar. Scattering clouds, parameterized using the EddySed model (Ackerman & Marley 2001; Mollière et al. 2020), produce low vertical diffusion (K_{zz}) and a high sedimentation parameter ($f_{\rm sed}$). The values for K_{zz} are below 5, the "minimum" value for the baseline model in Ackerman & Marley (2001). The sedimentation efficiency $f_{\rm sed} \simeq 12$–16 implies a very thin cloud layer, contrasting with results for the red, low surface gravity planet HR 8799 e ($f_{\rm sed} \simeq 2$; Mollière et al. 2020). These $f_{\rm sed}$ values are much higher than those typically invoked to model

BDs of similar spectral types (1–4; Saumon & Marley 2008; Stephens et al. 2009) and, similar to the derived abundances, appear to indicate a deficiency in the retrieval framework. These cloud parameters merely encode the opacity necessary to fit the data within the retrieval framework. This problem appears related to our inability to capture the likely near-solar abundance of the BD with our retrievals (see Section 6.3); from a data standpoint alone, the SPHERE *Y–J* data appears to have the strongest influence on the derived cloud and abundance parameters. As discussed below, it could be that, with an implausibly thin cloud layer, the retrieval is attempting to mimic the discontinuous abundance profile of iron hydride (e.g., the "rainout" effect), which can have a large impact on the derived metallicities [Fe/H] for mid-L-type BDs (Rowland et al. 2023).

Nevertheless, taken at face value a high $f_{\rm sed}$ and low K_{zz} points to a less vertically extended, less vigorously mixed cloud layer; this is not unreasonable given the age of the system. It is generally expected that the age and vertical extent of clouds are interrelated (with younger objects hosting more vertically extended, vigorously mixed clouds) and that this effect plays a large role in the delay of the L–T transition in young substellar objects (see Faherty 2018, Section 5 and references therein). This hypothesis could be tested with 3–5 μm observations of the object, where the spectrum is more sensitive to disequilibrium chemistry effects that can place constraints on vertical mixing, and certainly with observations of the 10 μm silicate feature, although these seem infeasible at present for an object at this close a separation.

We have seen the effect the choice of cloud model has on the retrieved P-T structure as a consequence. In general, the EddySed cloud model arrives at a solution where a deeper iron cloud deck (near the altitude of the isothermal knee in the gray slab retrieval) and then a silicate cloud (near the altitude of the gray slab cloud) appear. This overcompensation from the gray cloud retrieval, forcing a change in the P-T structure to mimic opacity that could as easily be described by a physical cloud deck, might indicate that the gray cloud assumption oversimplifies the structure of the clouds on HD 72946 B, if these clouds do exist. This is supported by the findings of other retrieval studies, which indicate a qualitatively similar set of clouds (a deep iron cloud and a higher silicate cloud) that best fit the 1–20 μm spectrum of isolated BDs (Burningham et al. 2017, 2021). However, as we have noted, the assumption of radiative–convective equilibrium (which results in a large temperature gradient) precludes the alternative solution: the BD is relatively cloudless (or, the clouds do not play a strong role in producing NIR opacity) and the shape of the NIR spectra is produced by a lower temperature gradient generated by fingering convection arising from a chemical gradient (Tremblin et al. 2015, 2016, 2019). Since our data does not probe these deeper pressure layers, the results of this retrieval experiment are somewhat ambiguous.

The EddySed retrievals arrived at similar abundances of iron and enstatite (a log abundance ratio near zero) when the abundances were unconstrained. When they were constrained to the stellar values, the posterior distribution of the abundance ratio appeared multimodal, with a mode near zero, but with a more dominant mode favoring iron grains by nearly a factor of 100, pushing against the prior boundary. This can be seen in the poor fit of these spectra to the SPHERE *Y–J* spectrophotometry, as an abundant iron cloud layer and low metallicity results in a flattened *Y–J* slope, whereas it would appear that a significant fraction of FeH, Na, and K opacity are necessary to reproduce the observed shape of the SPHERE spectrum.

6.2. Retrieved Abundances

It is expected that a high-mass BD like HD 72946 B would have formed from the same molecular cloud as its host, and therefore HD 72946 B would have effectively the same abundances as HD 72946 A ([Fe/H] $= 0.036 \pm 0.023$, C/O $= 0.51 \pm 0.05$). We note that, as discussed in Section 3, our stellar abundance determination should be viewed as a lower limit on O, indicating that the C/O for the star could be lower than 0.51. With the dynamical mass prior, we find that in the absence of a source of cloud opacity, the retrieval is driven toward very high [Fe/H] $= 0.86 \pm 0.05$ compared to the stellar value. Cloudy retrievals (either with or without a dynamical mass prior) with uniform abundance priors estimate C/O $\simeq 0.58 \pm 0.02$, and high [Fe/H] $\simeq 0.7 \pm 0.1$. This C/O is systematically higher than the stellar value, by 1σ–2σ. Placing a prior on the abundances (both [Fe/H] and C/O) based on the stellar values results in a systematically lower retrieved C/O and an overall worse fit to the SPHERE *Y–J* data. In light of our uncertain stellar oxygen abundance determination, it is feasible that these retrieved C/O could be consistent with the stellar value, in which case the quality of the SPHERE *Y–J* spectrum (particularly the overall slope) would be called into question. These inconclusive abundance retrieval results are necessarily overshadowed by the well-fit, solar-abundance BT-Settl model, and appear therefore to indicate a deficiency in the retrieval framework.

Previous studies have indicated that parameterized P-T profiles can bias the retrieval of most bulk properties (Wang et al. 2022; Rowland et al. 2023), and so future work should explore freely parameterized P-T profiles. Our retrievals assume chemical equilibrium, which could bias our retrieved C/O and [Fe/H] if there is significant mixing in the atmosphere. Rowland et al. (2023) indicate that nonuniform abundances of FeH (iron hydride) can cause systematic errors in the retrieval of surface gravity and parameterized abundances, regardless of its P-T structure, for L-type BDs. While our chemical equilibrium treatment should produce a nonuniform abundance, simulating this rainout effect, chemical disequilibrium could potentially disrupt these abundance profiles and result in a biased metallicity. It seems more likely that disequilibrium could affect the derived abundances of the major oxygen- and carbon-bearing species, which can currently be explored with our retrieval framework. Future work will explore this. In Figure 8, we see that varying the prior assumptions of our retrievals has the strongest impact on the quality of the fit to the SPHERE spectrophotometry, where water and FeH (iron hydride) has a large role in shaping the slope of the low-resolution spectrum, which could be impacted by biases induced by the data reduction or instrumental throughput treatment. Future work should investigate whether implementing the changes to retrievals mentioned above on the spectrum of HD 72946 B results in more reasonable [Fe/H], and whether a dynamical mass might improve the efficacy of these improved retrievals.

6.3. Dynamical Mass Prior for Atmospheric Retrieval

We investigated leveraging the dynamical mass (Section 4) and well-determined properties of the host star (Section 3) when comparing retrieval fits. We find an informative, though not necessarily satisfying, set of results. As with the self-consistent model grid, without a dynamical mass prior, the derived surface gravities and radii and therefore the derived masses from the spectral fits produce wildly inconsistent masses, as the retrieval struggles to reconcile the interplay between surface gravity, clouds, and molecular opacities with a large number of free parameters.

Comparing the uniform abundance prior retrievals, but only examining the variation of our prior assumption on the dynamical mass, we find that the dynamical mass prior retrieval obtains a lower $\log(g)$, radius, and metallicity than the uninformative mass prior retrieval, but a marginally higher C/O. Notably, the posterior distributions on the P-T profile, cloud, and other nuisance parameters show no effective differences between the two retrievals. This is evidence that the inclusion of the dynamical mass prior does not effectively constrain the P-T structure or cloud properties of this retrieval. It is not unprecedented, from a physical standpoint, that the inclusion of a dynamical mass prior in our retrieval does not effectively constrain the Ackerman & Marley (2001) cloud model parameters. Based on a microphysics model Gao et al. (2018) found that $f_{\rm sed}$ is dependent on K_{zz} but not on gravity, for a constant K_{zz}; of course, outside of the EddySed model, K_{zz} is not necessarily constant, and could even be constructed to depend on gravity via mixing-length-theory arguments (Mukherjee et al. 2022).

The systematic shift in $\log(g)$, radius, [Fe/H], and C/O is noticeable in the full posterior distribution plot (Figure 12 in Appendix A), and is related to the scale height of the atmosphere, which the dynamical mass prior does indirectly constrain. Without this prior, in order to fit the data, the scale height of the atmosphere decreases, decreasing the radius, and the number density in the photosphere increases, which affects the cross sections implied by the abundances. That is, left free, the retrieval appears to probe too deep, resulting in smaller radii and higher $\log(g)$, which affects the determination of the abundances. It is evident that, currently, a dynamical mass prior is useful insofar as it helps isolate or determine retrieval deficiencies, but it is not apparent whether future improvements to the retrieval framework (or to atmospheric modeling in general) will necessitate the inclusion of a dynamical mass prior.

6.4. In Context

In a similar retrieval analysis, Xuan et al. (2022) showed that their high-resolution ($R \sim 35{,}000$) KPIC spectra of a cloudy BD are not sensitive to clouds, because the clouds contribute the most opacity at lower altitudes. While the high resolution constrains C/O by probing the K-band CO bandhead at higher pressures, their retrieved abundances appear independent of a variety of cloud assumptions. This is not the case for their retrieval using only low-resolution data. We find a qualitatively similar result here. From our analysis it appears that the VLTI/GRAVITY spectrum ($R \sim 500$) of HD 72946 B is able to probe a wide enough range of pressures above the cloud deck to enable a retrieval of the C/O independent of the cloud parameterization.

It remains unclear whether a dynamical mass prior dramatically improves the retrieval of cloud properties for this BD. We can safely argue that, assuming the EddySed cloud model, a parameterized P-T profile, and chemical equilibrium, a dynamical mass prior does not appear to strongly constrain the cloud or P-T profile parameters for a high surface gravity L-type object. This is in part also due to the lack of MIR data on HD 72946 B, where the spectral signatures of silicate grains exhibit strong wavelength dependence, and are able to constrain the cloud properties directly (Burningham et al. 2021). This motivates future studies of more widely separated benchmark BDs (with strong dynamical mass constraints) with JWST/MIRI. Coupling direct observations of silicate absorption in benchmark BDs with retrievals or improving retrievable parametric cloud models might yet constrain the composition, shape, and size distribution of cloud particles in these L-type substellar companions. In the short term, implementing a free P-T profile and nonuniform abundance profiles for key molecules might improve the accuracy of the physical parameters derived from the retrieved spectrum of HD 72946 B. Observations from GRAVITY can quickly refine the orbital parameters of detected companions, even those on longer-period orbits, and can therefore shape the landscape of viable targets for future benchmark/atmosphere studies.

Regardless of the exact cloud composition or parameterization, or of the structure of the P-T profile, the C/O of the object appears to be in agreement with the stellar value to within 2σ, indicating the efficacy of the GRAVITY spectrum in constraining C/O. This result is important insofar as it benchmarks these retrievals on an object with a dynamical mass and expected C/O, indicating the reliability of the C/O (but perhaps not the [Fe/H]) derived from similar retrievals for HR 8799 e and β Pic b within the scope of the ExoGRAVITY Large Program (Gravity Collaboration et al. 2020; Mollière et al. 2020).

7. Summary

In this paper we present new observations of the BD companion HD 72946 B from VLTI/GRAVITY. The observations yielded four astrometric points with impressive precision and a moderate-resolution $R = 500$ K-band spectrum of the companion. The precise astrometry enabled us to refine the orbit of the companion and improve the dynamical mass measurement, when fit jointly with RVs and absolute astrometry. The enhanced resolution in the K band allowed for a precise observation of the carbon monoxide bandhead at 2.3 μm, even at a separation of only $\sim$125 mas.

We also present an updated joint isochronal and spectral analysis of the host using archival photometry and visible light spectroscopy. We determined the mass ($0.97 \pm 0.01\,M_{\odot}$), age ($2.67^{+0.25}_{-0.49}$ Gyr), and elemental abundances (Tables 3 and 7) for the star self-consistently. These parameters helped to inform our understanding of the BD companion's evolution, orbit, and composition.

We compared two orbit fitting schemes, where we considered fits with and without absolute astrometry from the HGCA and the reported Gaia eDR3 system parallax, and found that the inclusion of absolute astrometry brought the error on the dynamical mass to 1.1%. With this precise a mass, HD 72946 B will be a crucial system on which to test evolutionary models for substellar objects in the near future. Future work should investigate whether the existing GRAVITY astrometry has the precision to constrain the influence of the widely separated (10″) comoving stellar binary HD 72945 AB on the orbit of HD 72946 AB, as was attempted without the GRAVITY data set in Brandt et al. (2021).

We compared the observed spectrum of HD 72946 B to the BT-Settl-CIFIST grid of self-consistent, microphysical cloudy model atmospheres. Based on our forward model fits, the object has an effective temperature of ∼1750 K, a log(g) of ∼5.4, and a radius of ∼0.86 R_J. We then constructed free retrievals with petitRADTRANS. We investigated the effect of a dynamical mass prior on the retrieved atmosphere. We briefly compared the interdependence of the retrieved P-T profiles on our cloud model, verifying that the observed spectrum could be fit with either a reduced temperature gradient or a cloud deck.

The retrieval analysis presented here is only a sample of what can be explored using the now well-determined properties of the HD 72946 system. Our investigation indicates the need to include rainout of FeH in our retrieval setup in the future. Future work could benefit from measuring the H-band and MIR silicate features of the companion. Future work utilizing different retrieval codes under different assumptions (for instance, chemical disequilibrium) could also benefit from a dynamical mass prior, as could the application of additional self-consistent forward models.

VLTI/GRAVITY observations of exoplanets have already proven the instrument's unique capability to observe multi-planet interactions (Lacour et al. 2021), precisely determine substellar C/O (Mollière et al. 2020; Nowak et al. 2020; Kammerer et al. 2021), and dramatically refine a companion's orbital parameters (Wang et al. 2020; Kammerer et al. 2021). With our observations of HD 72946 B we have demonstrated the instrument's capacity to conduct similar studies of benchmark BDs at even higher signal-to-noise ratios. Atmospheric studies of these objects can inform our understanding of the best practices for determining the elemental abundances for exoplanets, which are key quantities for constraining planetary formation pathways and histories.

Acknowledgments

W.O.B. would like to thank Jacob Hamer for his input regarding the age estimates of the HD 72946 system, and Sagnick Mukherjee for helpful discussions regarding clouds. We thank the anonymous referee for the helpful review. The authors sincerely thank the Paranal Observatory astronomers and local staff for their tremendous support in completing these observations.

Based on observations collected at the European Southern Observatory under ESO programme(s) 1104.C-0651(B), 1103.B-0626(D).

T.S. acknowledges support from the Netherlands Organisation for Scientific Research (NWO) through grant VI.Veni.202.230.

This work used the Dutch national e-infrastructure with the support of the SURF Cooperative using grant No. EINF-1620.

S.L. acknowledges the support of the French Agence Nationale de la Recherche (ANR), under grant ANR-21-CE31-0017 (project ExoVLTI).

This work is based on spectral data retrieved from the ELODIE archive at Observatoire de Haute-Provence (OHP), available at http://atlas.obs-hp.fr/elodie. It is also based on data retrieved from the SOPHIE archive at OHP, available at http://atlas.obs-hp.fr/sophie.

This research has made use of the VizieR catalog access tool, CDS, Strasbourg, France (DOI:10.26093/cds/vizier).

This research has made use of the Jean-Marie Mariotti Center Aspro service.

This publication makes use of data products from 2MASS, which is a joint project of the University of Massachusetts and the Infrared Processing and Analysis Center/California Institute of Technology, funded by the National Aeronautics and Space Administration and the National Science Foundation.

This work has made use of data from the European Space Agency mission Gaia (https://www.cosmos.esa.int/gaia), processed by the Gaia Data Processing and Analysis Consortium (DPAC; https://www.cosmos.esa.int/web/gaia/dpac/consortium). Funding for the DPAC has been provided by national institutions, in particular the institutions participating in the Gaia Multilateral Agreement.

W.O.B. acknowledges that the Johns Hopkins University (JHU) occupies the unceded land of the Piscataway people, and acknowledges the Piscataway community, their elders both past and present, and future generations. JHU (http://web.archive.org/web/20220816104243/http://trujhu.org/index.php/about-us/land-acknowledgement/) was founded on and presides over the exclusions and erasures of many people, a fact no less true for being contentious, and one that bears repeating even in long acknowledgment sections.

W.O.B. graciously acknowledges their cat, Morgoth, for her "encouragement."

Appendix A
Posterior Distributions

This appendix contains the posterior distributions of the various multidimensional models fit to the data throughout this paper. Table 5 contains the median and 1σ CI on the posterior distribution of orbits fit excluding absolute astrometry, described in Section 4, and Table 6 lists the same for the orbit fit including absolute astrometry. Figure 10 illustrates the comparative posterior distribution of orbital elements between the two orbit fits in Tables 5 and 6. Figure 11 plots the comparative posterior distribution of BT-Settl-CIFIST model spectra fit to HD 72946 B. Figure 12 plots the comparative posterior distribution of petitRADTRANS retrievals using the EddySed cloud model recorded in Table 4.

Table 5
Orbital Parameters Inferred for HD 72946 B Excluding Absolute Astrometry

Parameter	Description	Median	Lower 1σ CI	Upper 1σ CI
a (au)	Semimajor axis	6.487	−0.059	0.058
e	Eccentricity	0.497	−0.006	0.005
i (rad)	Inclination	1.102	−0.004	0.004
ω (rad)	Argument of periastron	4.343	−0.005	0.005
Ω (rad)	Longitude of ascending node	6.190	−0.004	0.005
τ (decl. cal. yr)	Next periastron passage after $\tau_{\rm ref}$ [a]	2028.164	−0.126	0.129
π (mas)	Parallax	38.798	−0.382	0.388
$\gamma_{\rm ELODIE}$ (km s^{-1})	RV offset term	29.427	−0.006	0.006
$\sigma_{\rm ELODIE}$ (km s^{-1})	RV jitter term	0.026	−0.003	0.004
$\gamma_{\rm SOPHIE}$ (km s^{-1})	RV offset term	29.514	−0.007	0.006
$\sigma_{\rm SOPHIE}$ (km s^{-1})	RV jitter term	0.014	−0.003	0.004
M_B ($M_\odot$)	Mass of B	0.067	−0.001	0.001
M_A ($M_\odot$)	Mass of A	0.985	−0.026	0.026

Notes. We report the median and 68% CI on each parameter derived from the posterior visualized in Figure 10. This orbit analysis did not include absolute astrometry.
[a] We set $\tau_{\rm ref} = 2020.0$.

Table 6
Orbital Parameters Inferred for HD 72946 B including Absolute Astrometry

Parameter	Description	Median	Lower 1σ CI	Upper 1σ CI
a (au)	Semimajor axis	6.462	−0.029	0.030
e	Eccentricity	0.498	−0.005	0.005
i (rad)	Inclination	1.102	−0.003	0.003
ω (rad)	Argument of periastron	4.343	−0.005	0.005
Ω (rad)	Longitude of ascending node	6.189	−0.004	0.005
τ (decl. cal. yr)	Next periastron passage after $\tau_{\rm ref}$ [a]	2028.154	−0.080	0.083
π (mas)	Parallax	38.981	−0.010	0.010
$\gamma_{\rm ELODIE}$ (km s^{-1})	RV offset term	29.427	−0.006	0.006
$\sigma_{\rm ELODIE}$ (km s^{-1})	RV jitter term	0.026	−0.003	0.004
$\gamma_{\rm SOPHIE}$ (km s^{-1})	RV offset term	29.514	−0.007	0.006
$\sigma_{\rm SOPHIE}$ (km s^{-1})	RV jitter term	0.014	−0.003	0.004
M_B ($M_\odot$)	Mass of B	0.066	−0.001	0.001
M_A ($M_\odot$)	Mass of A	0.975	−0.013	0.013

Notes. We report the median and 68% CI on each parameter derived from the posterior visualized in Figure 10. This orbit analysis included absolute astrometry from the HGCA.
[a] We set $\tau_{\rm ref} = 2020.0$.

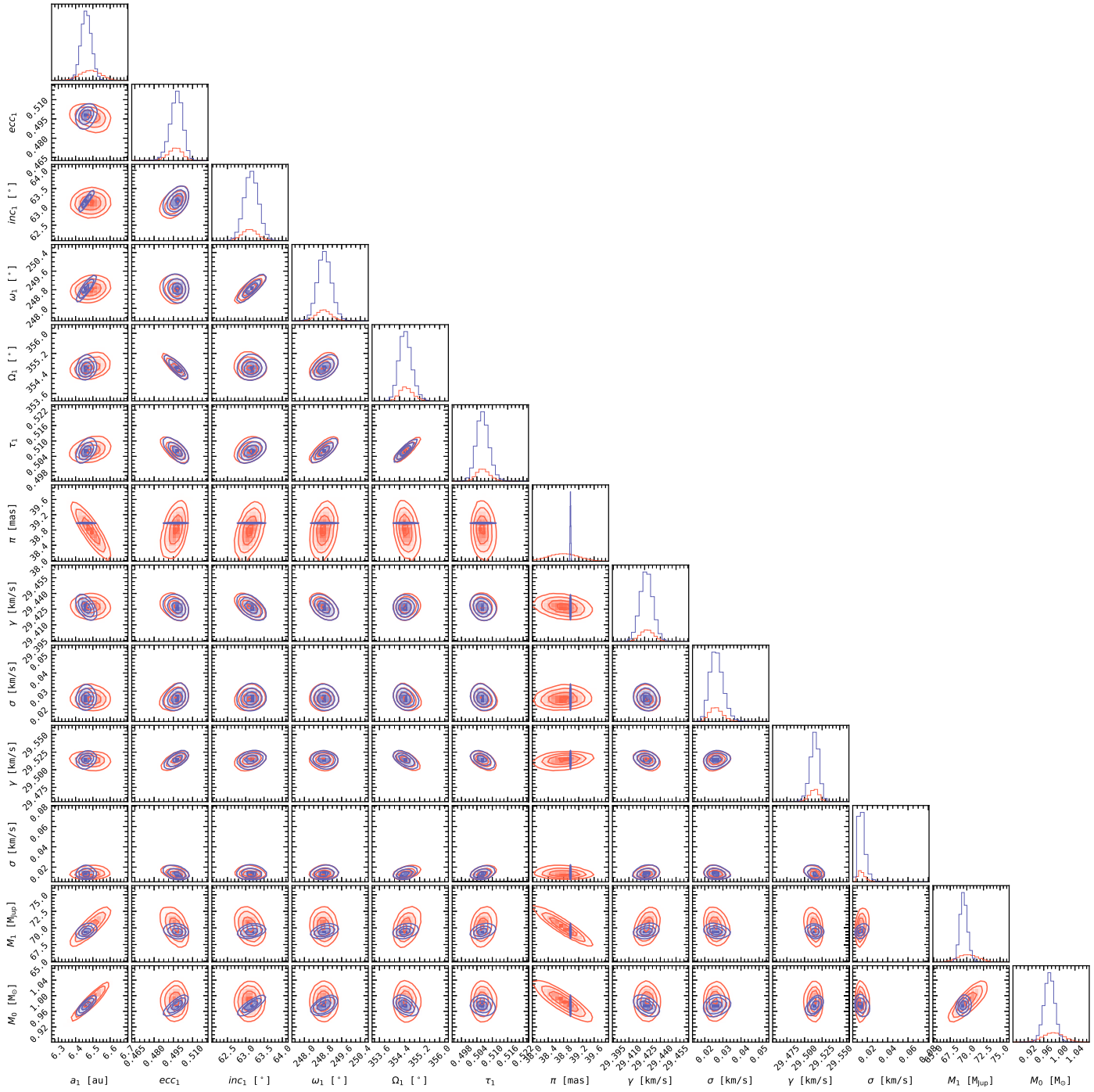

Figure 10. The posterior distributions of orbit fits to the HD 72946 system. The red contours and histograms plot the posterior for the "no absolute astrometry" fit, while the blue contours and histograms plot the posterior for the fit including absolute astrometry.

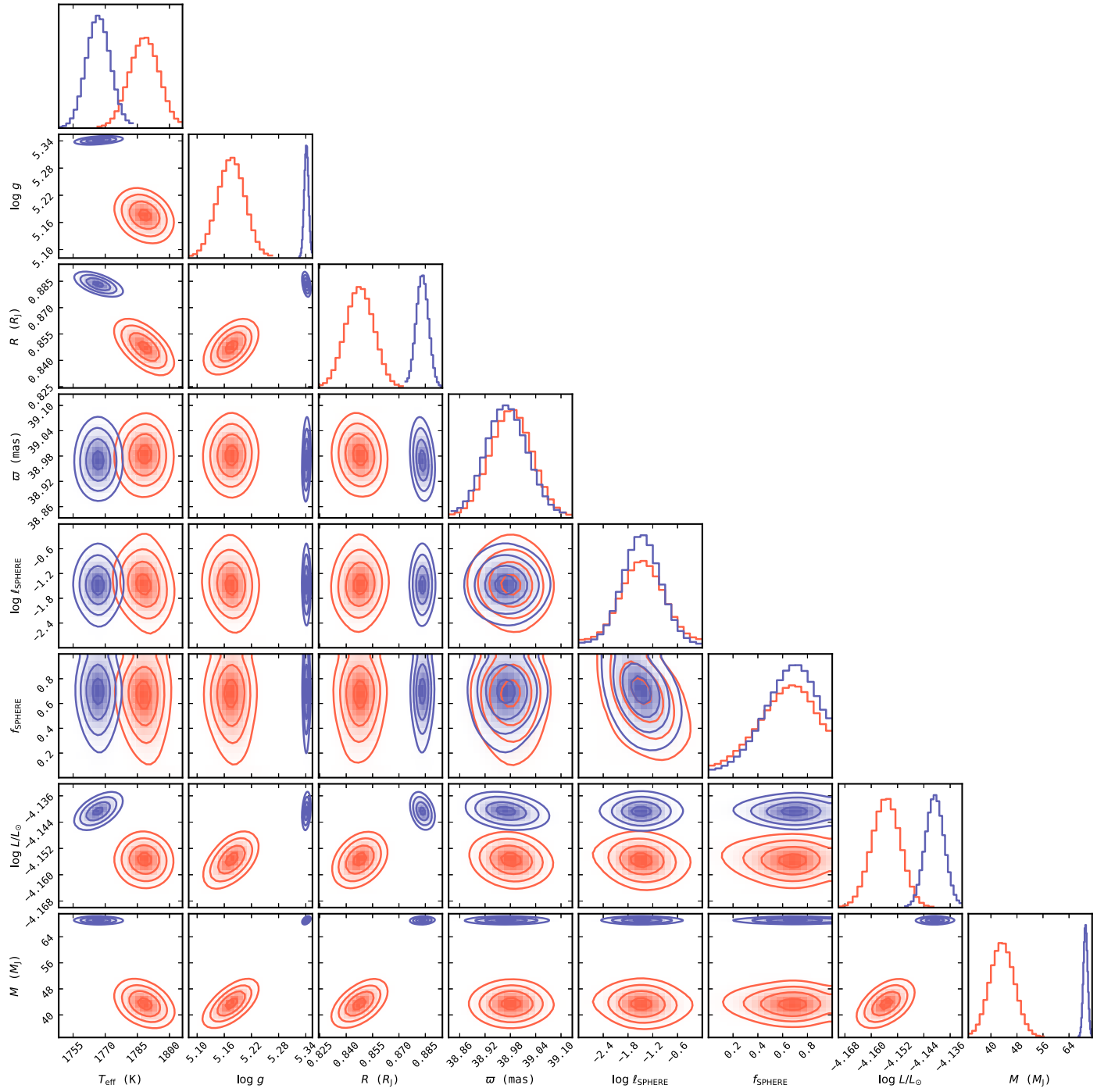

Figure 11. The posterior distribution of `BT-Settl` model spectra fit to observations of HD 72946 B. The dark blue, generally narrower posteriors correspond to the fit with a prior on the mass of the object equivalent to the dynamical mass derived in Section 4, while the red, generally wider posteriors correspond to the free mass fit. Other than the nuisance parameters (parallax, and the Gaussian process "correlation matrix" fit to the SPHERE/IFU data), the parameters are generally normally distributed and well constrained, but distinct between the two cases. Notably, the dynamical mass constrains the log(g) and radius to higher values, leading to a lower temperature.

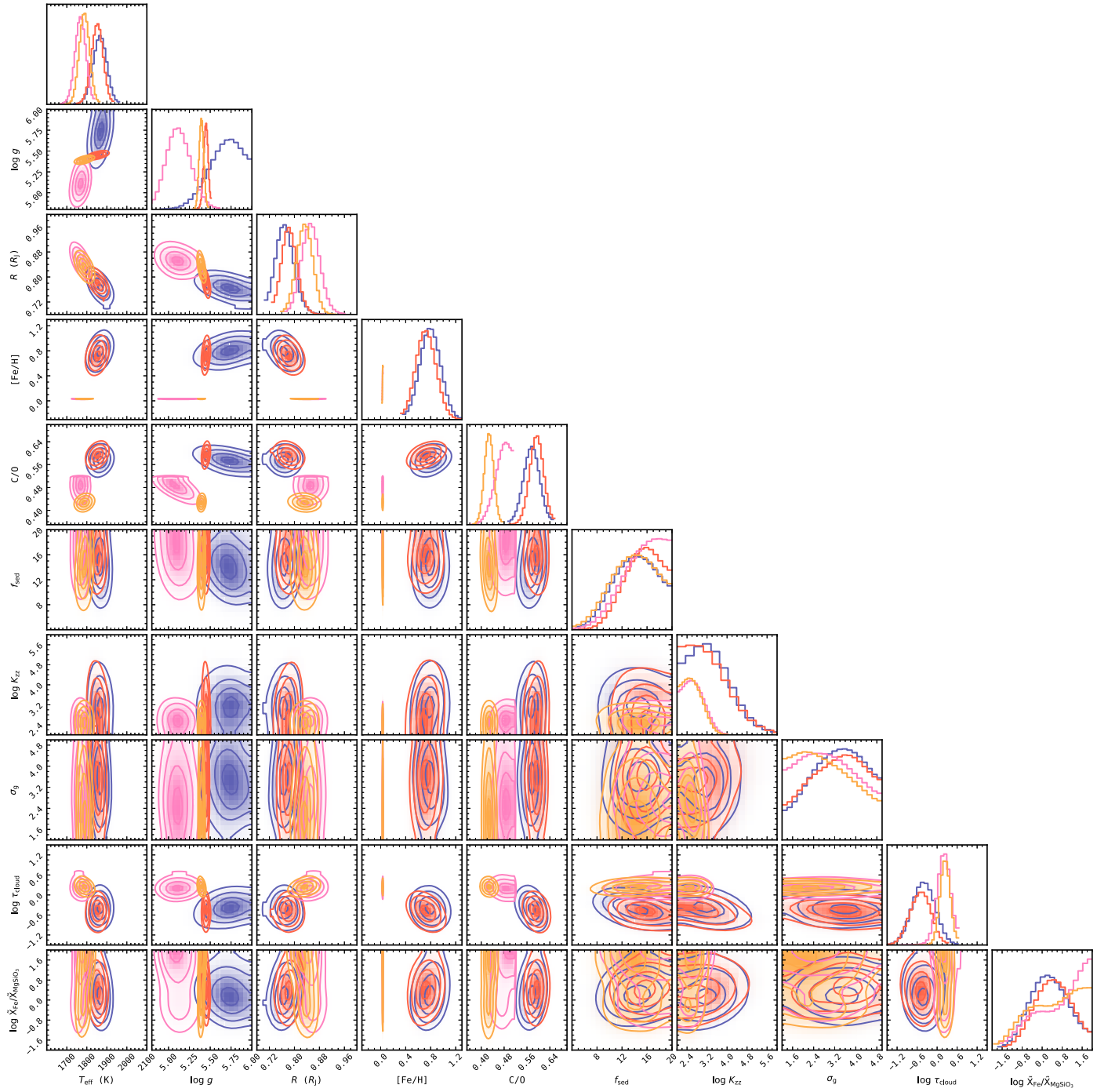

Figure 12. The posterior distributions of four `petitRADTRANS` retrievals with the EddySed cloud model. Each retrieval implements the three-part P-T profile but the priors on the mass and on the abundances ([Fe/H] and C/O) are varied between retrievals. As in Figure 8, the red contours plot the posterior assuming a uniform mass and abundance prior, the blue contours the posterior assuming a prior on the dynamical mass but a uniform abundance prior, the pink contours the posterior assuming a uniform mass but Gaussian priors on the stellar abundances, and the orange contours the posterior assuming Gaussian priors on both the dynamical mass and the stellar abundances.

Appendix B
Host Star

This appendix contains both the table of derived abundances for the host star HD 72946 A, Table 7, and Figure 13 illustrating the scaled `BT-NextGen` model stellar atmosphere fit to the literature photometry recorded in Table 3.

Table 7
Elemental Abundances for HD 72946 A

Species	$A(X)$	(X/H)	$\sigma_{(X/H)}$	(X/Fe)	$\sigma_{(X/Fe)}$	n
LTE abundances						
C I	8.369	−0.091	0.038	−0.127	0.054	2
O I	8.660	…	…	…	…	1
Na I	6.191	−0.029	0.078	−0.065	0.048	4
Mg I	7.600	0.050	0.094	0.014	0.054	5
Al I	6.409	−0.021	0.015	−0.057	0.022	2
Si I	7.580	0.070	0.081	0.034	0.025	14
S I	7.107	−0.013	0.000	−0.049	0.037	1
Ca I	6.373	0.073	0.043	0.037	0.035	11
Sc I	3.121	−0.019	0.022	−0.055	0.034	3
Sc II	3.167	0.027	0.212	−0.009	0.078	10
Sc I	3.121	−0.019	0.022	−0.055	0.034	3
Sc II	3.167	0.027	0.212	−0.009	0.078	10
Ti I	4.951	−0.019	0.100	−0.055	0.046	17
Ti II	5.076	0.106	0.069	0.070	0.041	13
V I	3.993	0.093	0.061	0.057	0.044	9
Cr I	5.696	0.076	0.056	0.040	0.037	14
Cr II	5.741	0.121	0.155	0.085	0.074	7
Mn I	5.307	−0.113	0.105	−0.149	0.049	8
Fe I	7.491	0.031	0.069	−0.005	0.026	63
Fe II	7.521	0.061	0.072	0.025	0.047	18
Ni I	6.297	0.097	0.067	0.061	0.026	18
Cu I	4.173	−0.007	0.076	−0.043	0.058	3
Zn I	4.647	0.087	0.098	0.051	0.074	3
Sr I	2.724	−0.106	0.000	−0.142	0.055	1
Y II	2.360	0.150	0.058	0.114	0.056	4
Zr II	2.631	0.041	0.166	0.005	0.123	3
Ba II	2.478	0.208	0.062	0.172	0.050	4
La II	1.331	0.221	0.000	0.185	0.033	1
Ce II	1.776	0.196	0.148	0.160	0.110	3
Nd II	1.592	0.172	0.072	0.136	0.061	3
Dy II	1.132	0.032	0.000	−0.004	0.033	1
1D non-LTE abundances						
Al I	6.368	−0.062	…	−0.131	…	1
Ca I	6.034	−0.266	0.07	−0.335	…	2
Fe I	7.524	0.064	0.072	…	…	63
Fe II	7.547	0.087	0.063	…	…	18
3D non-LTE abundances						
C I	8.352	−0.108	0.077	−0.177	…	5
Additional abundance ratios of interest						
$(Fe/H)_{1D\ non\text{-}LTE} = 0.069 \pm 0.080$						
$((C + O)/H) = -0.121 \pm 0.038$						
$(C/O) = -0.061 \pm 0.038$						
$C/O_{1D\ LTE} = 0.512^{+0.047}_{-0.043}$						
$Mg/Si_{1D\ LTE} = 1.047 \pm 0.124$						

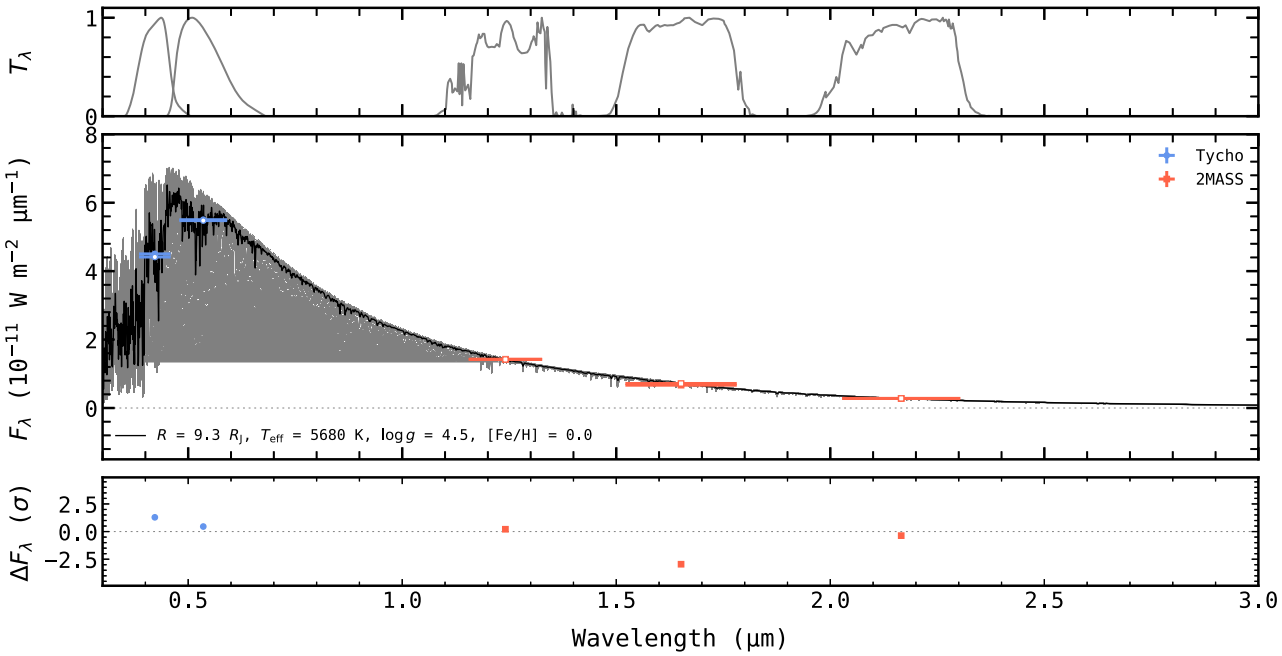

Figure 13. A `BT-NextGen` model spectrum of HD 72946 A with parameters based on our host star analysis scaled to the archival photometry of the star. Transmission profiles for the photometric filters are plotted in the upper panel. The flux density of the spectrum is plotted in the middle panel, with the best fit in black and 30 random samples in gray, and the measured photometry overlaid as colored circles and squares. The residuals to the scaling fit are shown in the bottom panel.

ORCID iDs

William O. Balmer https://orcid.org/0000-0001-6396-8439
Laurent Pueyo https://orcid.org/0000-0003-3818-408X
Tomas Stolker https://orcid.org/0000-0002-5823-3072
Henrique Reggiani https://orcid.org/0000-0001-6533-6179
A.-L. Maire https://orcid.org/0000-0002-2591-4138
S. Lacour https://orcid.org/0000-0002-6948-0263
P. Mollière https://orcid.org/0000-0003-4096-7067
D. Sing https://orcid.org/0000-0001-6050-7645
N. Pourré https://orcid.org/0000-0001-9431-5756
S. Blunt https://orcid.org/0000-0002-3199-2888
J. J. Wang https://orcid.org/0000-0003-0774-6502
E. Rickman https://orcid.org/0000-0003-4203-9715
J. Kammerer https://orcid.org/0000-0003-2769-0438
Th. Henning https://orcid.org/0000-0002-1493-300X
K. Ward-Duong https://orcid.org/0000-0002-4479-8291
R. Asensio-Torres https://orcid.org/0000-0003-2990-0726
M. Benisty https://orcid.org/0000-0002-7695-7605
A. Bohn https://orcid.org/0000-0003-1401-9952
M. Bonnefoy https://orcid.org/0000-0001-5579-5339
W. Brandner https://orcid.org/0000-0003-1939-6351
F. Cantalloube https://orcid.org/0000-0002-3968-3780
P. Caselli https://orcid.org/0000-0003-1481-7911
B. Charnay https://orcid.org/0000-0003-0977-6545
V. Christiaens https://orcid.org/0000-0002-0101-8814
A. Eckart https://orcid.org/0000-0001-6049-3132
R. Garcia Lopez https://orcid.org/0000-0002-2144-0991
R. Genzel https://orcid.org/0000-0002-2767-9653
S. Gillessen https://orcid.org/0000-0002-5708-0481
J. H. Girard https://orcid.org/0000-0001-8627-0404
S. Hinkley https://orcid.org/0000-0001-8074-2562
S. Hippler https://orcid.org/0000-0002-3912-6108
M. Horrobin https://orcid.org/0000-0001-5451-7847
P. Kervella https://orcid.org/0000-0003-0626-1749
L. Kreidberg https://orcid.org/0000-0003-0514-1147
D. Lutz https://orcid.org/0000-0003-0291-9582
J. D. Monnier https://orcid.org/0000-0002-3380-3307
T. Ott https://orcid.org/0000-0003-1572-0396
T. Paumard https://orcid.org/0000-0003-0655-0452
G. Perrin https://orcid.org/0000-0003-0680-0167
L. Rodet https://orcid.org/0000-0002-1259-3312
J. Shangguan https://orcid.org/0000-0002-4569-9009
T. Shimizu https://orcid.org/0000-0002-2125-4670
L. J. Tacconi https://orcid.org/0000-0002-1485-9401
E. F. van Dishoeck https://orcid.org/0000-0001-7591-1907
A. Vigan https://orcid.org/0000-0002-5902-7828
F. Vincent https://orcid.org/0000-0002-3855-0708
J. Woillez https://orcid.org/0000-0002-2958-4738

References

Ackerman, A. S., & Marley, M. S. 2001, ApJ, 556, 872
Aguilera-Gómez, C., Ramírez, I., & Chanamé, J. 2018, A&A, 614, A55
Allard, F. 2014, in IAU Symp. 299, Exploring the Formation and Evolution of Planetary Systems, ed. M. Booth, B. C. Matthews, & J. R. Graham (Cambridge: Cambridge Univ. Press), 271
Allard, F., Guillot, T., Ludwig, H.-G., et al. 2003, in IAU Symp. 211, Brown Dwarfs, ed. E. Martín (San Francisco, CA: ASP), 325
Allard, F., Homeier, D., & Freytag, B. 2011, in ASP Conf. Ser. 448, 16th Cambridge Workshop on Cool Stars, Stellar Systems, and the Sun, ed. C. Johns-Krull, M. K. Browning, & A. A. West (San Francisco, CA: ASP), 91
Allard, F., Homeier, D., & Freytag, B. 2012, RSPTA, 370, 2765
Allard, F., Homeier, D., Freytag, B., Schaffenberger, W., & Rajpurohit, A. S. 2013, MSAIS, 24, 128
Amarsi, A. M., Lind, K., Asplund, M., Barklem, P. S., & Collet, R. 2016, MNRAS, 463, 1518
Amarsi, A. M., Lind, K., Osorio, Y., et al. 2020, A&A, 642, A62
Amarsi, A. M., Nissen, P. E., & Skúladóttir, Á. 2019, A&A, 630, A104
Asplund, M., Amarsi, A. M., & Grevesse, N. 2021, A&A, 653, A141
Baraffe, I., Homeier, D., Allard, F., & Chabrier, G. 2015, A&A, 577, A42
Bate, M. R. 2009, MNRAS, 392, 590
Blunt, S., Wang, J. J., Angelo, I., et al. 2020, AJ, 159, 89
Bonavita, M., Fontanive, C., Gratton, R., et al. 2022, MNRAS, 513, 5588
Bonnefoy, M., Chauvin, G., Rojo, P., et al. 2010, A&A, 512, A52
Borysow, A., Frommhold, L., & Moraldi, M. 1989, ApJ, 336, 495
Borysow, A., Jorgensen, U. G., & Fu, Y. 2001, JQSRT, 68, 235

Borysow, J., Frommhold, L., & Birnbaum, G. 1988, ApJ, 326, 509
Boss, A. P. 1997, Sci, 276, 1836
Bouchy, F., Ségransan, D., Díaz, R. F., et al. 2016, A&A, 585, A46
Bowler, B. P. 2016, PASP, 128, 102001
Brandt, G. M., Dupuy, T. J., Li, Y., et al. 2021, AJ, 162, 301
Brandt, T. D. 2018, ApJS, 239, 31
Brandt, T. D. 2021, ApJS, 254, 42
Brandt, T. D., Dupuy, T. J., & Bowler, B. P. 2019, AJ, 158, 140
Brown-Sevilla, S. B., Maire, A. L., Mollière, P., et al. 2023, A&A, 673, A98
Buchner, J. 2019, PASP, 131, 108005
Buchner, J. 2021, JOSS, 6, 3001
Buchner, J., Georgakakis, A., Nandra, K., et al. 2014, A&A, 564, A125
Burningham, B., Faherty, J. K., Gonzales, E. C., et al. 2021, MNRAS, 506, 1944
Burningham, B., Marley, M. S., Line, M. R., et al. 2017, MNRAS, 470, 1177
Burrows, A., Hubbard, W. B., Lunine, J. I., & Liebert, J. 2001, RvMP, 73, 719
Burrows, A., Marley, M., Hubbard, W. B., et al. 1997, ApJ, 491, 856
Carnall, A. C. 2017, arXiv:1705.05165
Casagrande, L., Lin, J., Rains, A. D., et al. 2021, MNRAS, 507, 2684
Casagrande, L., Schönrich, R., Asplund, M., et al. 2011, A&A, 530, A138
Chabrier, G., & Baraffe, I. 2000, ARA&A, 38, 337
Choi, J., Dotter, A., Conroy, C., et al. 2016, ApJ, 823, 102
Chubb, K. L., Rocchetto, M., Yurchenko, S. N., et al. 2021, A&A, 646, A21
Gravity Collaboration, Abuter, R., Accardo, M., et al. 2017, A&A, 602, A94
Gravity Collaboration, Nowak, M., Lacour, S., et al. 2020, A&A, 633, A110
Cushing, M. C., Rayner, J. T., & Vacca, W. D. 2005, ApJ, 623, 1115
Cushing, M. C., Roellig, T. L., Marley, M. S., et al. 2006, ApJ, 648, 614
Czekala, I., Andrews, S. M., Mandel, K. S., Hogg, D. W., & Green, G. M. 2015, ApJ, 812, 128
Dotter, A. 2016, ApJS, 222, 8
Duchêne, G., Oon, J. T., De Rosa, R. J., et al. 2023, MNRAS, 519, 778
Dupuy, T. J., & Liu, M. C. 2012, ApJS, 201, 19
Dupuy, T. J., & Liu, M. C. 2017, ApJS, 231, 15
Faherty, J. K. 2018, in Handbook of Exoplanets, ed. H. J. Deeg & J. A. Belmonte (Berlin: Springer), 188
Fernandes, C. S., Van Grootel, V., Salmon, S. J. A. J., et al. 2019, ApJ, 879, 94
Feroz, F., & Hobson, M. P. 2008, MNRAS, 384, 449
Feroz, F., Hobson, M. P., & Bridges, M. 2009, MNRAS, 398, 1601
Feroz, F., Hobson, M. P., Cameron, E., & Pettitt, A. N. 2019, OJAp, 2, 10
Filippazzo, J. C., Rice, E. L., Faherty, J., et al. 2015, ApJ, 810, 158
Fontanive, C., Biller, B., Bonavita, M., & Allers, K. 2018, MNRAS, 479, 2702
Fontanive, C., Mužić, K., Bonavita, M., & Biller, B. 2019, MNRAS, 490, 1120
Foreman-Mackey, D., Hogg, D. W., Lang, D., & Goodman, J. 2013, PASP, 125, 306
Fouesneau, M., Frémat, Y., Andrae, R., et al. 2023, A&A, 674, A28
Franson, K., Bowler, B. P., Bonavita, M., et al. 2023, AJ, 165, 39
Franson, K., Bowler, B. P., Brandt, T. D., et al. 2022, AJ, 163, 50
Gaia Collaboration, Brown, A. G. A., Vallenari, A., et al. 2018, A&A, 616, A1
Gaia Collaboration, Brown, A. G. A., Vallenari, A., et al. 2021, A&A, 649, A1
Gaia Collaboration, Prusti, T., de Bruijne, J. H. J., et al. 2016, A&A, 595, A1
Gao, P., Marley, M. S., & Ackerman, A. S. 2018, ApJ, 855, 86
Gonzales, E. C., Burningham, B., Faherty, J. K., et al. 2020, ApJ, 905, 46
Green, R. M. 1985, Spherical Astronomy (Cambridge: Cambridge Univ. Press)
Grether, D., & Lineweaver, C. H. 2006, ApJ, 640, 1051
Henning, T., & Stognienko, R. 1996, A&A, 311, 291
Høg, E., Fabricius, C., Makarov, V. V., et al. 2000, A&A, 355, L27
Jaeger, C., Molster, F. J., Dorschner, J., et al. 1998, A&A, 339, 904
Johansson, S., Litzén, U., Lundberg, H., & Zhang, Z. 2003, ApJL, 584, L107
Kammerer, J., Lacour, S., Stolker, T., et al. 2021, A&A, 652, A57
Knapp, G. R., Leggett, S. K., Fan, X., et al. 2004, AJ, 127, 3553
Kratter, K. M., Murray-Clay, R. A., & Youdin, A. N. 2010, ApJ, 710, 1375
Lacour, S., Dembet, R., Abuter, R., et al. 2019, A&A, 624, A99
Lacour, S., Wang, J. J., Nowak, M., et al. 2020, Proc. SPIE, 11446, 114460o
Lacour, S., Wang, J. J., Rodet, L., et al. 2021, A&A, 654, L2
Lapeyrere, V., Kervella, P., Lacour, S., et al. 2014, Proc. SPIE, 9146, 91462D
Li, Y., Brandt, T. D., Brandt, G. M., et al. 2023, MNRAS, 522, 5622
Li, Y., Kouwenhoven, M. B. N., Stamatellos, D., & Goodwin, S. P. 2016, ApJ, 831, 166
Line, M. R., Teske, J., Burningham, B., Fortney, J. J., & Marley, M. S. 2015, ApJ, 807, 183
Luck, R. E. 2017, AJ, 153, 21
Luck, R. E., & Heiter, U. 2006, AJ, 131, 3069
Lueber, A., Kitzmann, D., Bowler, B. P., Burgasser, A. J., & Heng, K. 2022, ApJ, 930, 136
Ma, B., & Ge, J. 2014, MNRAS, 439, 2781
Magg, E., Bergemann, M., Serenelli, A., et al. 2022, A&A, 661, A140
Maire, A. L., Baudino, J. L., Desidera, S., et al. 2020, A&A, 633, L2
Manjavacas, E., Bonnefoy, M., Schlieder, J. E., et al. 2014, A&A, 564, A55
Marley, M. S., Saumon, D., Visscher, C., et al. 2021, ApJ, 920, 85
Meléndez, J., Schirbel, L., Monroe, T. R., et al. 2014, A&A, 567, L3
Mollière, P., Molyarova, T., Bitsch, B., et al. 2022, ApJ, 934, 74
Mollière, P., Stolker, T., Lacour, S., et al. 2020, A&A, 640, A131
Mollière, P., Wardenier, J. P., van Boekel, R., et al. 2019, A&A, 627, A67
Morton, T. D., 2015 isochrones: Stellar model grid package, Astrophysics Source Code Library, ascl:1503.010
Moultaka, J., Ilovaisky, S. A., Prugniel, P., & Soubiran, C. 2004, PASP, 116, 693
Mukherjee, S., Fortney, J. J., Batalha, N. E., et al. 2022, ApJ, 938, 107
Nelson, B. E., Ford, E. B., Buchner, J., et al. 2020, AJ, 159, 73
Nowak, M., Lacour, S., Lagrange, A. M., et al. 2020, A&A, 642, L2
Öberg, K. I., Murray-Clay, R., & Bergin, E. A. 2011, ApJL, 743, L16
Padoan, P., & Nordlund, Å 2004, ApJ, 617, 559
Patience, J., King, R. R., De Rosa, R. J., et al. 2012, A&A, 540, A85
Paxton, B., Bildsten, L., Dotter, A., et al. 2011, ApJS, 192, 3
Paxton, B., Cantiello, M., Arras, P., et al. 2013, ApJS, 208, 4
Paxton, B., Marchant, P., Schwab, J., et al. 2015, ApJS, 220, 15
Paxton, B., Schwab, J., Bauer, E. B., et al. 2018, ApJS, 234, 34
Paxton, B., Smolec, R., Schwab, J., et al. 2019, ApJS, 243, 10
Peretti, S., Ségransan, D., Lavie, B., et al. 2019, A&A, 631, A107
Phillips, M. W., Tremblin, P., Baraffe, I., et al. 2020, A&A, 637, A38
Placco, V. M., Sneden, C., Roederer, I. U., et al. 2021, RNAAS, 5, 92
Reggiani, H., Schlaufman, K. C., Healy, B. F., Lothringer, J. D., & Sing, D. K. 2022, AJ, 163, 159
Richard, C., Gordon, I. E., Rothman, L. S., et al. 2012, JQSRT, 113, 1276
Rickman, E. L., Matthews, E., Ceva, W., et al. 2022, A&A, 668, A140
Rickman, E. L., Ségransan, D., Hagelberg, J., et al. 2020, A&A, 635, A203
Rowland, M. J., Morley, C. V., & Line, M. R. 2023, ApJ, 947, 6
Saumon, D., & Marley, M. S. 2008, ApJ, 689, 1327
Scott, A., & Duley, W. W. 1996, ApJS, 105, 401
Skrutskie, M. F., Cutri, R. M., Stiening, R., et al. 2006, AJ, 131, 1163
Sneden, C., Bean, J., Ivans, I., Lucatello, S., & Sobeck, J., 2012 MOOG: LTE line analysis and spectrum synthesis, Astrophysics Source Code Library, ascl:1202.009
Sneden, C., Lawler, J. E., Cowan, J. J., Ivans, I. I., & Den Hartog, E. A. 2009, ApJS, 182, 80
Sneden, C., Lawler, J. E., den Hartog, E. A., & Wood, M. E. 2016, IAUFM, 29A, 287
Sneden, C. A. 1973, PhD thesis, Univ. of Texas, Austin
Spina, L., Meléndez, J., Karakas, A. I., et al. 2016, A&A, 593, A125
Squicciarini, V., Gratton, R., Janson, M., et al. 2022, A&A, 664, A9
Stamatellos, D., Hubber, D. A., & Whitworth, A. P. 2007, MNRAS, 382, L30
Stamatellos, D., & Whitworth, A. P. 2009, MNRAS, 392, 413
Stephens, D. C., Leggett, S. K., Cushing, M. C., et al. 2009, ApJ, 702, 154
Stolker, T., Quanz, S. P., Todorov, K. O., et al. 2020, A&A, 635, A182
STScI Development Team, 2018 synphot: Synthetic photometry using Astropy, Astrophysics Source Code Library, ascl:1811.001
Suárez, G., & Metchev, S. 2022, MNRAS, 513, 5701
Suárez, G., & Metchev, S. 2023, MNRAS, 523, 4739
Teske, J. K., Cunha, K., Smith, V. V., Schuler, S. C., & Griffith, C. A. 2014, ApJ, 788, 39
Thorngren, D., & Fortney, J. J. 2019, ApJL, 874, L31
Tody, D. 1986, Proc. SPIE, 627, 733
Tody, D. 1993, in ASP Conf. Ser. 52, Astronomical Data Analysis Software and Systems II, ed. R. J. Hanisch, R. J. V. Brissenden, & J. Barnes (San Francisco, CA: ASP), 173
Tremblin, P., Amundsen, D. S., Chabrier, G., et al. 2016, ApJL, 817, L19
Tremblin, P., Amundsen, D. S., Mourier, P., et al. 2015, ApJL, 804, L17
Tremblin, P., Padioleau, T., Phillips, M. W., et al. 2019, ApJ, 876, 144
Umbreit, S., Burkert, A., Henning, T., Mikkola, S., & Spurzem, R. 2005, ApJ, 623, 940
Vacca, W. D., Cushing, M. C., & Rayner, J. T. 2003, PASP, 115, 389
Vos, J. M., Faherty, J. K., Gagné, J., et al. 2022, ApJ, 924, 68
Vousden, W. D., Farr, W. M., & Mandel, I. 2016, MNRAS, 455, 1919
Wang, J., Kolecki, J. R., Ruffio, J.-B., et al. 2022, AJ, 163, 189
Wang, J. J., Ginzburg, S., Ren, B., et al. 2020, AJ, 159, 263
Wang, J. J., Vigan, A., Lacour, S., et al. 2021, AJ, 161, 148
Xuan, J. W., Wang, J., Ruffio, J.-B., et al. 2022, ApJ, 937, 54
Yana Galarza, J., Meléndez, J., Lorenzo-Oliveira, D., et al. 2019, MNRAS, 490, L86
Zhang, Z. H., Burgasser, A. J., Gálvez-Ortiz, M. C., et al. 2019, MNRAS, 486, 1260